Maria Gombotz, BSc.

Ion Transport and Electrochemical Stability of Low Dimensional Fluorine Anion Conductors

MASTERARBEIT

zur Erlangung des akademischen Grades
Diplom-Ingenieurin
Masterstudium Technical Chemistry

eingereicht an der
Technischen Universität Graz

Betreuer
Dr. Ilie Hanzu
Univ.-Prof. Dr.rer.nat Martin Wilkening

Institut für die chemische Technologie von Materialien

Graz, August 2017

Danksagung

Während der Erarbeitung dieser Arbeit durfte ich viel Unterstützung von Seiten meiner Betreuer und KollegInnen erfahren, was in dieser Form sicher nicht selbstverständlich ist. Ein aufrichtiges Danke an Univ.-Prof. Dr.rer.nat. Martin Wilkening, der mir ermöglichte diese Arbeit in seiner Gruppe zu erstellen. Bei Dr. Ilie Hanzu möchte ich mich für die Unterstützung bei sämtlichen elektrochemischen Messungen bedanken und bei Dipl.-Ing. Stefan Breuer und Veronika Pregartner für die Hilfe bei den Impedanzmessungen und für ihr offenes Ohr wenn ich Probleme hatte. Danke auch an Dipl.-Ing. Isabel Hanghofer für die Hilfe mit dem Bau der Festkörperzellen und an Dipl.-Ing. Sarah Lunghammer für die großartige Unterstützung im Bereich der NMR.

Mein aufrichtiger Dank gilt der gesamten Arbeitsgruppe, die meine Zeit am ICTM sehr bereichert hat.

Dieser Arbeit ist ein fünf Jahre lang dauerndes Studium vorangegangen. Während dieser Zeit waren Katharina, Philipp, Thomas, Sebastian und Stefanie die beste Gesellschaft die ich mir wünschen konnte. Dank ihren kreativen Methoden jede Vorlesung, jeden Labortag und jede Pause abwechslungsreich zu gestalten, ist mir die Freude am Studium immer geblieben. Ein riesiges Danke auch an Kilian, für alles.

Zuletzt ein großes Danke an meine Eltern ohne die diese Arbeit nie entstanden wäre, da sie mir nicht nur dieses Studium finanziell ermöglicht haben, sondern mich auch unermüdlich und in jeder Hinsicht unterstützen.

Statutory Declaration

I declare that I have authored this thesis independently, that I have not used other than the declared sources / resources, and that I have explicitly indicated all material which has been quoted either literally or by content from the used sources. The text document uploaded to TUGRAZonline is identical to the present master's thesis.

Eidesstattliche Erklärung

Ich erkläre an Eides statt, dass ich die vorliegende Arbeit selbstständig verfasst, andere als die angegebenen Quellen/Hilfsmittel nicht benutzt, und die den benutzten Quellen wörtlich und inhaltlich entnommenen Stellen als solche kenntlich gemacht habe. Das in TUGRAZonline hochgeladene Textdokument ist mit der vorliegenden Masterarbeit identisch.

Graz _____ _____

Date, Datum Signature, Unterschrift

Abstract

In a world with constantly increasing population and thus with rising energy demand, various energy storage systems gain importance. Most attention is turned to rechargeable Li-ion batteries since the 90'ies[10], whereas in the last years several other systems, for example based on Na^+[33], are investigated further. In 2011 also the principle of a rechargeable system, based on fluorine as charge carrier was experimentally proven by Reddy et al.[33]. This is however a recent development and there are numerous question which remain unanswered, concerning the cathode as well as anode material and the electrolyte of these systems.

In the course of this work, the possible solid state electrolytes $BaSnF_4$ and $RbSn_2F_5$, both exhibiting a 2-dimensional structure, as well as $La_{0.9}Ba_{0.1}F_{2.9}$, were mechanochemically synthesised and characterised by XRD, impedance spectroscopy and polarisation measurements. The electrochemical stability was examined using cyclic voltammetry. Furthermore, on the one hand, the relaxation times T_1 and $T_{1\rho}$ were determined to gain an insight in the time dependent processes of ion conduction. On the other hand, ^{19}F, ^{119}Sn and ^{87}Rb Magic Angle Spinning Nuclear Magnetic Resonance (MAS NMR) was carried out to determine the number of ion sites in all F^--ion conductors.

The solid state electrolytes were subsequently used with elemental lithium as anode and BiF_3 as cathode in Fluorine Ion Batteries (FIBs). Cells with $La_{0.9}Ba_{0.1}F_{2.9}$ could only be discharged, whereas charging was not possible. Therefore a set-up with LiF as anode and Bi as cathode was tried. However, the cycling was also very difficult and the cells survived for only one cycle. Contrary to that, cells based on the electrolyte $RbSn_2F_5$ were reversibly cycled up to 10 times. Similar reversible cycling of FIBs was reported in literature[33][34] for only three times up to date.

Kurzfassung

In einer Welt mit immer weiter steigenden Bevölkerungszahlen und dem dadurch erhöhten Energiebedarf, gewinnen verschiedenste Energiespeichersysteme konstant an Bedeutung. Ein besonderes Augenmerk liegt dabei schon seit den 1990er Jahren[10] auf wiederaufladbaren Li-Ionen Batterien, wobei in den letzten Jahren auch zahlreiche andere Systeme, z.B. basierend auf Na^+[33], in den Fokus der Wissenschaft rücken. 2011 wurde auch erstmals das Prinzip einer wiederaufladbaren Zelle basierend auf Fluor als Ladungsträger experimentell von Reddy et al.[33] bewiesen. Aufgrund der relativ geringen Zeitspanne bis heute, gibt es noch zahlreiche unbeantwortete Fragen bezüglich Kathoden-, Anodenmaterial und Elektrolyt dieser Systeme.

Im Zuge dieser Arbeit lag das Hauptaugenmerk auf der mechanochemischen Synthese und Charakterisierung der Fluor-Anionen Leiter und möglichen Festkörperelektrolyte $BaSnF_4$ und $RbSn_2F_5$, welche beide eine zweidimensionale Struktur aufweisen, als auch $La_{0.9}Ba_{0.1}F_{2.9}$, mittels Röntgenbeugung, Impedanzspektroskopie und Polarisationsmessungen. Die elektrochemische Stabilität wurde mittels Cyclovoltammetrie untersucht. Des Weiteren wurden zum Einen die Relaxationszeiten T_1 als auch $T_{1\rho}$ bestimmt, um einen Einblick in den zeitlichen Ablauf des Ionentransports zu bekommen, und zum Anderen wurde ^{19}F, ^{119}Sn und ^{87}Rb Magic Angle Spinning Kernspinresonanzspektroskopie (MAS NMR) durchgeführt, um Einblick in die Anzahl der verschiedenen Plätze der Ionen zu erlangen.

Alle Festkörperelektrolyte wurden im Anschluss mit elementarem Lithium als Anode und BiF_3 als Kathode getestet, wobei gezeigt werden konnte, dass Zellen basierend auf $La_{0.9}Ba_{0.1}F_{2.9}$ als Elektroylt entladen werden können, jedoch das schlechtleitende LiF, welches sich wahrscheinlich an der Elektrolyt-Anode-Berührungsfläche entwickelt, ein Aufladen der Zelle verhindert. Daher wurde eine weitere Kombination mit LiF als Anode und Bi als Kathode getestet, was ebenfalls nur zu einem möglichen Entladezyklus führte. Im Gegensatz dazu konnten Zellen mit $RbSn_2F_5$ als Festkörperelektrolyt bis zu 10 mal sowohl ent- als auch geladen werden, wobei in diesem Fall sehr wahrscheinlich eine Reaktion zwischen Li-Anode und Elektrolyt stattfindet. Eine ähnliche reversible Zyklisierung wurde bisher in der Literatur[33][34] erst dreimal nachgewiesen.

Contents

Abbreviations

AC	Alternating Current
DC	Direct Current
DSC	Differential Scanning Calorimetry
EDX	Energy Dispersive X-ray spectroscopy
EIS	Electrochemical Impedance Spectroscopy
FIB	Fluorine Ion Battery
FID	Free Induction Decay
FT	Fourier Transformation
GCPL	Galvanostatic Cycling with Potential Limitation
ICSD	Inorganic Crystal Structure Database
MAS NMR	Magic Angle Spinning Nuclear Magnetic Resonance
NMR	Nuclear Magnetic Resonance
PEG	Polyethylene Glycol
rf-pulse	radio frequency pulse
SEM	Scanning Electron Microscopy
SNR	Signal-to-Noise Ratio
STA	Simultaneous Thermal Analysis
XRD	X-Ray Diffraction

1 Theoretical Aspects

1.1 F^--ion conductors

In the following three sections an overview on the synthesised F^--ion conductors, concerning structural features, ionic conductivity and, if published to date, NMR results are given. Additionally the influence of the synthesis route on the previous mentioned characteristics is pointed out, whenever sufficient data is available.

1.1.1 Fluorite-type structure

The best ionic conductor, not only in this crystal family of the fluorite type (CaF_2-structure, Fm-3m), but also of all fluorides is $PbSnF_4$, closely followed by $BaSnF_4$[8]. $BaSnF_4$ can exist in two modifications, the cubic and tetragonal one[4]. Cubic $BaSnF_4$, which is present e.g. after mechanochemical synthesis, can be transformed by annealing into the tetragonal form, which is more conductive and has a layered structure[32]. The tetragonal modification can also be achieved directly using more conventional synthesis routes, as solid state or precipitation reaction[28]. Patro et al. showed in 2011[28] that the synthesis route has a considerable influence on the ionic conductivity. The highest ionic conductivity at 20 °C ($3.2 \cdot 10^{-4}$ S·cm^{-1}) is achieved via mechanochemical milling and a subsequent annealing step, mainly due to the comparably small crystal size of approximately 24 nm, hence more defects and the induced micro-strain.

The high ionic conductivity in this compound can be explained with some special features concerning the layered structure, which were investigated by the means of ^{119}Sn and ^{19}F MAS NMR[9]. $BaSnF_4$ is composed of alternating layers of Ba and Sn in the following manner: · · ·BaBaSnSnBaBaSnSn· · ·, as illustrated in Fig. 1.1.

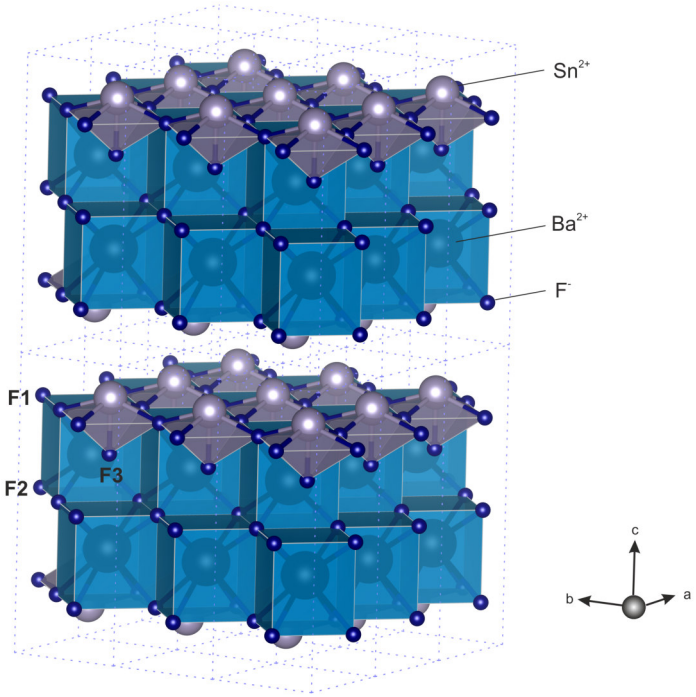

Fig. 1.1: Visualisation of the 2D F^--ion conduction in $BaSnF_4$ with F1 - 3 indicating the three different F^--ion sites.

No fluorine ions are present in the Sn - Sn - layer, due to the lone pairs of Sn pointing towards this layer, and furthermore the fluorine ions in the Ba - Ba - layer were found to be significant less mobile, compared to the ones in the Ba - Sn - layer. Therefore the ionic conduction takes place mainly in the Ba - Sn - layer, giving the tetragonal $BaSnF_4$ the 2 - dimensional conduction structure.

1.1.2 Tysonite-type structure

The second of the three crystal structures these fluoride conductors adopt, is the tysonite type ($P\text{-}3c1$), which is mainly featured by rare-earth fluorides with the formula RF_3 (R = La, Ce, Pr, Nd)[36]. Within this family, BaF_2-doped LaF_3 ($La_{1-x}Ba_xF_{3-x}$), as shown in Fig. 1.2, was synthesised, characterised and further used as solid state electrolyte in FIBs[36].

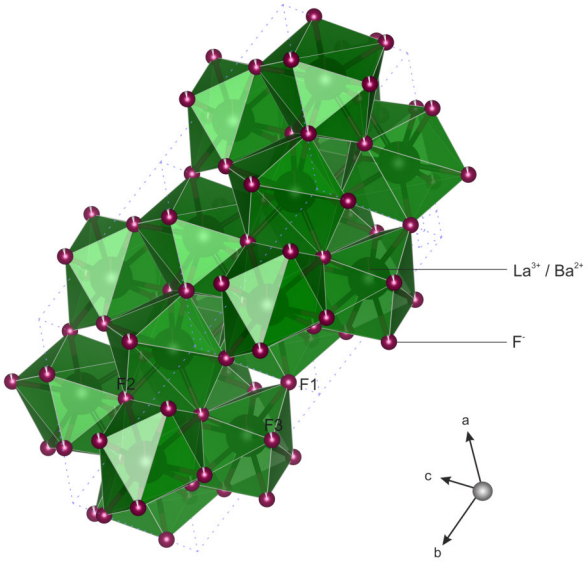

Fig. 1.2: Visualisation of the F^--ion conduction in LaF_3, with La^{3+} being partially substituted by Ba^{2+}. F1 - 3 are indicating the three different F^--ion sites.

Among the various synthesised compositions[36], $La_{0.9}Ba_{0.1}F_{2.9}$ was found to offer the highest conductivity and lowest activation energy, with values of $2.81{\cdot}10^{-4}$ S·cm^{-1} and 0.55 eV at 160 °C. A further increase of the doping concentration lead to lower conductivities, which may have its origin in the formation of vacancy clusters. Further ^{19}F MAS NMR illustrated a higher bulk conductivity in $La_{0.9}Ba_{0.1}F_{2.9}$ compared to grain boundary conductivity. In order to reduce the number of grain boundaries, different annealing experiments were carried out, which lead indeed to a slightly higher conductivity ($9.06{\cdot}10^{-4}$ S·cm^{-1} at 160 °C) with the drawback of creating additional impurity phases.

Therefore unannealed $La_{0.9}Ba_{0.1}F_{2.9}$ was chosen as the most convenient compound having tysonite structure for all experiments in this work.

1.1.3 MSn_2F_5-type structure

$RbSn_2F_5$ belongs to the family of the pseudo-binary system MF-SnF_2, where M is a monovalent cation, for example Rb^+, K^+, Na^+ or Cs^+[38]. Within this family $RbSn_2F_5$[1] offers the highest conductivity followed by KSn_2F_5[3] and $NaSn_2F_5$[29].

Up to now $RbSn_2F_5$ was only prepared by solid state reaction[38] or hydrothermal synthesis in aqueous solution, which was first reported in literature in 1964 by Donaldson and O'Donoghue[11]. In 1987 the structure of KSn_2F_5, to which $RbSn_2F_5$ is isomorphous, was resolved as being trigonal with the space group $P\bar{3}$ (Z=3)[7].

In Fig.1.3 the structure of $RbSn_2F_5$ is illustrated and clearly shows the 2-dimensional nature of this compound.

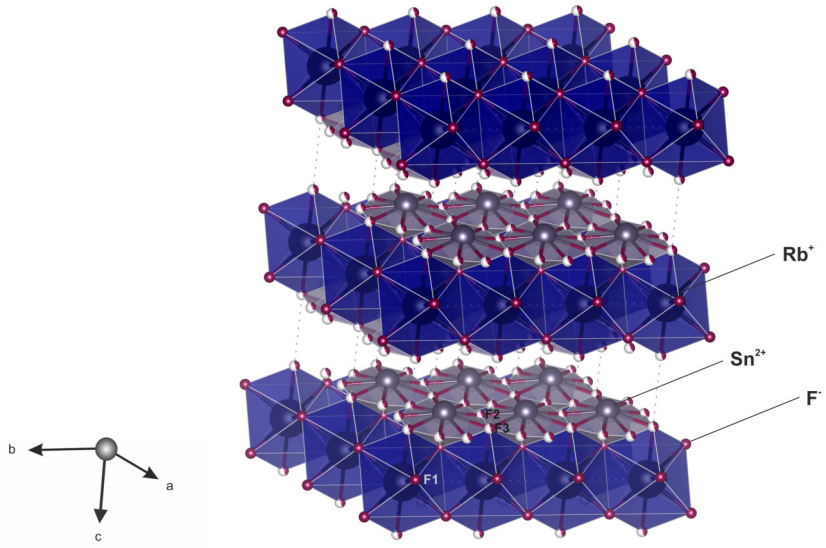

Fig. 1.3: Visualisation of the 2D F^--ion conduction in $RbSn_2F_5$ with F1 - 3 indicating the three different F^--ion sites.

Later is was proven[39] that at a temperature of 95 °C the space group changes from $P\bar{3}$ (Z=3) to $P\bar{3}$ (Z=1). The phase transition temperature was detected with DSC, but no clear phase change was visible in the diffractogram of $RbSn_2F_5$ measured at different temperatures. Rather the reflections, corresponding to the [300] miller indices, shift to lower angles with increasing temperature, suggesting an expansion in the *ab*-plane. In contrast to that the reflection, corresponding to the [005] miller indices, shift to higher angles, indicating a contraction of the *c* plane. This phase change is also detectable in the conductivity isothermes, recorded via impedance spectroscopy, and translates into a sudden increase of conductivity at this temperature.

1.2 X-ray diffraction (XRD)

X-ray diffraction is a powerful, non destructive method to reveal not only the crystal structure and phase composition of a sample, but to gain also insight to several other material properties like grain size, stress and strain etc.[14] This method was routinely used to characterize the synthesised F^--ion conductors.

In the course of a XRD measurement, monochromatic X-rays are generated, hit the sample and get diffracted in a certain angle. To be more specific, the generation of monochromatic X-rays occurs in sealed X-ray tubes where electrons are emitted by the cathode and accelerated towards the anode, due to a voltage difference between them. When the electrons hit the anode, X-rays are generated which consist of bremsstrahlung and the characterisic X-ray radiation. After passing through an X-ray monochromator,

these X-rays strike the sample and are diffracted at certain angles, before hitting a detector. Destructive interference of diffracted X-rays leads to no detectable reflections, whereas constructive interference does. Constructive interference is given if Bragg's law 1.1 is valid.[14][17]

$$2 \cdot d \cdot sin\theta = n \cdot \lambda \tag{1.1}$$

where

d : Interplanar spacing
θ : Bragg angle
n : 1, 2, 3,..
λ : Wavelength

The geometrical representation of Bragg's law is illustrated in Fig. 1.4.

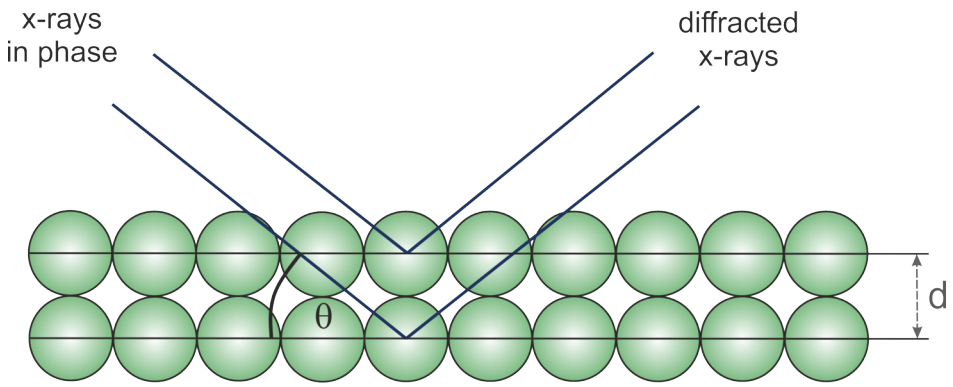

Fig. 1.4: Visualisation of Bragg s law, adapted from reference[24].

The outcome of a XRD measurement as described is a plot of intensity against 2θ. Not only the position of the reflection is important, but also the intensity which is for example influenced by the structure factor (in turn influenced by the symmetry of the crystal and the position of an atom in the unit cell). By comparing positions and intensity of all reflexes with data, available in several databases, e.g. the ICSD, the compound can be identified[14][17].

As already mentioned, not only the crystal structure and phase composition can be determined, but also other sample properties as the crystallite size. It must be noted, that this method is only suitable to estimate the crystallite size roughly, as the broadening of the reflection is affected by various factors, as the micro strain or spectral broadening.[24] Additionally impurities or minor phases can be hidden within broad reflections, especially in the case of nano-crystalline samples. To uncover these, solid-state NMR is a suitable method.[32]

1.3 Impedance Spectroscopy

As Electrochemical Impedance Spectroscopy is a widespread method and was used to determine the conductivity of all synthesised F^--ion conductors, this chapter[6][26] should give an overview of its most important features.

The resistance R [Ω] a system is showing when a current I [A], applied at a certain voltage U [V], is flowing through it, is defined via the well-known Ohm's law 1.2, which is only valid at all times in the case of an ideal resistor, where voltage and current are in phase.

$$R = \frac{U}{I} \tag{1.2}$$

The resistance can be defined also in a different way via Eq. 1.3.

$$R = \rho \cdot \frac{d}{A} \tag{1.3}$$

where

ρ : Resistivity [$\Omega\,$cm]
d : Thickness of the sample [cm]
A : Surface of the sample [cm^2]

The conductivity σ is simply defined as the reciprocal resistivity *i.e.* $\sigma = 1/\rho$. Even though the impedance is also defined as the ratio between voltage and current, it also counts in the phase shift between the entering voltage and the resulting current.

When the impedance is determined experimentally, an AC voltage signal with a certain amplitude is applied at different frequencies. The input voltage signal, which is dependent on time, is expressed with the following Eq. 1.4.

$$V(t) = V_a \cdot sin(\omega \cdot t) \tag{1.4}$$

where

$V(t)$: Applied voltage [V]
V_{a} : Voltage amplitude [V]
ω : Angular frequency [Hz]
t : Time [s]

The resulting current output, with different phase and amplitude, can be expressed in the same way as shown in Eq. 1.5.

$$I(t) = I_a \cdot sin(\omega \cdot t + \phi) \tag{1.5}$$

where

$I(t)$: Resulting current [A]
I_a : Current amplitude [A]
ω : Angular frequency [Hz]
t : Time [s]
ϕ : Phase shift

Fig. 1.5 is illustrating the phase shift ϕ between the applied voltage and the current response.

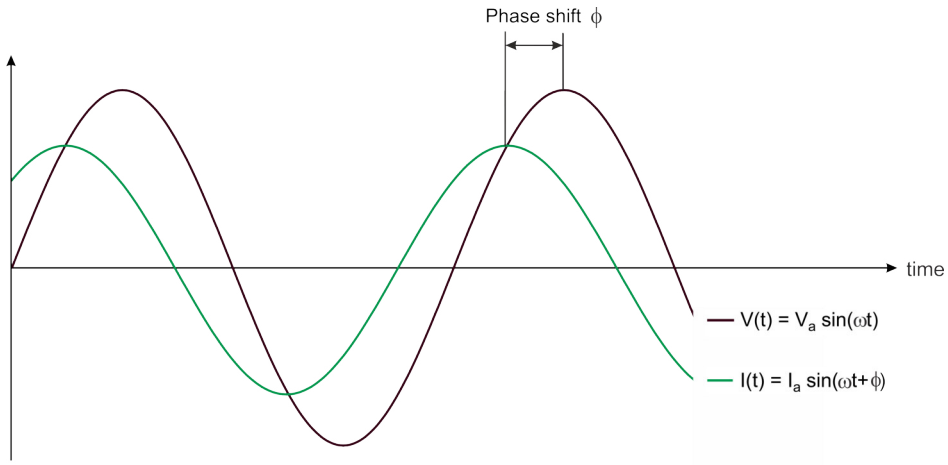

Fig. 1.5: Illustration of the phase shift ϕ between incoming voltage and outgoing current signal, during an impedance spectroscopy. Adapted from reference[26].

With the above stated equations, a new "Ohm's law" can be defined as shown in Eq. 1.6.

$$Z^* = \frac{V_a \cdot sin(\omega t)}{I_a \cdot sin(\omega t + \phi)} = \frac{V(t)}{I(t)} \tag{1.6}$$

where

Z^* : Complex impedance [Ω]
V_{a} : Voltage amplitude [V]
I_{a} : Current amplitude [A]
ω : Angular frequency [Hz]
t : Time [s]
ϕ : Phase shift [ϕ]
V_{t} : Voltage input [V]
I_{a} : Current output [A]

With the aid of the Euler's relationship ($\exp(\mathrm{i}\phi) = \cos(\phi) + \mathrm{i}\sin(\phi)$), it is possible to rewrite Eq. 1.6 to Eq. 1.7.

$$Z^* = Z' + iZ" \tag{1.7}$$

where

Z^* : Complex impedance [Ω]
$Z^{'}$: Real part [Ω]
$Z^{"}$: Imaginary part [Ω]

The complex impedance consists of two parts, the real and the imaginary part. The real part represents the resistance to the current flowing through a circuit, whereas the complex part stands for the ability to capacitively store electrical energy.

In order to finally calculate the real part of the conductivity[31], the specific complex impedance $\tilde{Z}_{\mathrm{S}}$ has to be determined with Eq. 1.8 first, for what the area A of the sample pellet and the distance d between the electrodes, which is equivalent to the height of the pellet, must be known.

$$\tilde{Z}_s = \tilde{Z} \cdot \frac{A}{d} = Z'_s - iZ''_s = \frac{1}{\tilde{\sigma}} \tag{1.8}$$

With the aid of the above stated variables, the real part of the conductivity can be calculated with Eq. 1.9, which is further used to plot conductivity isothermes and subsequently the Arrhenius plot.

$$\sigma' = \frac{Z'_s}{Z'^2_s + Z''^2_s} \tag{1.9}$$

1.3.1 Conductivity Isothermes

In order to visualise the DC-conductivity at different temperatures, the real part of the conductivity is plotted on a double (decimal) logarithm scale against the frequency as shown in Fig. 1.6.

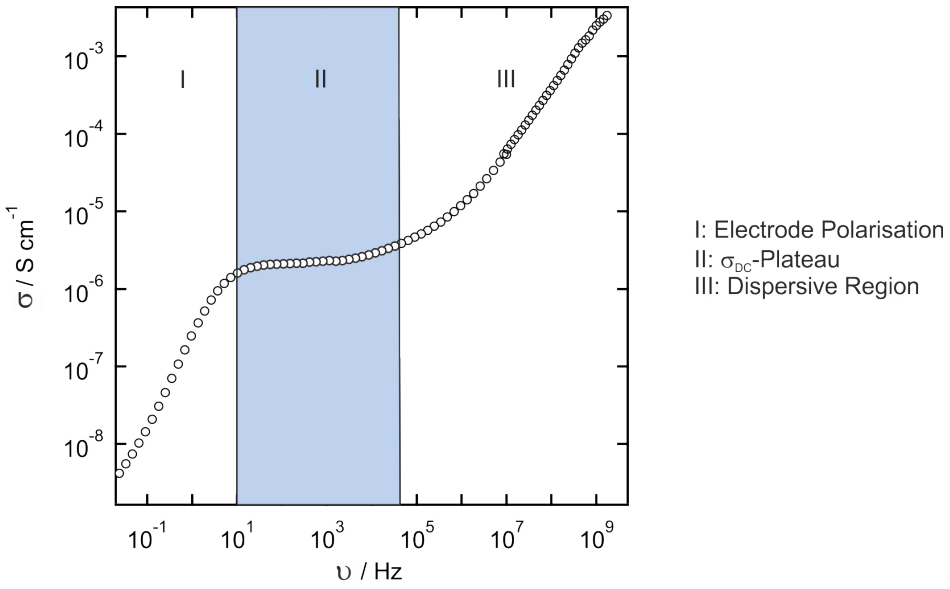

Fig. 1.6: Representation of the three different, characteristic regions of conductivity isothermes.

Usually the isothermes consist of three different regions marked I to III in Fig 1.6.

Region I, the electrode polarisation, occuring at low frequencies, shows the frequency range in which the ions accumulate or deplete at one of the blocking electrodes. Later in region II, commonly called the σ_{DC}-plateau, ions perform successful and long-range jumps between the different ion sites. At high frequencies, the dispersive region III marks a sector, where the ions perform forth and back motion within a very localized potential well, without successcul jumps between the different crystal sites.[13][32]

The conductivity at the σ_{DC}-plateau can be read off and is plotted as $\log(\sigma_{\mathrm{DC}} \cdot \mathrm{T})$ against the inverse temperature K^{-1}. The resulting diagram is called Arrhenius plot and the activation energy the ions require in order to perform successful jumps between the lattice sites, can be calculated out of the slope of the curves with Eq. 1.10.[25][5]

$$\sigma_{DC} = \frac{\sigma_0}{T} \cdot exp(\frac{E_A}{k_B T}) \tag{1.10}$$

where

T : Temperature [K]
E_{A} : Activation Energy [eV]
k_{B} : Boltzmann's constant [s]

1.4 Solid State NMR

^{19}F-, ^{119}Sn-, ^{87}Rb-MAS NMR and $T_{1,\,1\rho}$ measurements were carried out in the course of this work, therefore this chapter should give an insight in NMR spectroscopy[15][12]. As the field of NMR is very diverse and complex, this topic will only be discussed to the extent required to understand the basics of the measurements carried out and the conclusions drawn.

As the nucleus of an atom is charged and moving, it possesses a magnetic moment $\boldsymbol{\mu}$ (all vector quantities are given in bold letters) which is given by Eq. 1.11.

$$\boldsymbol{\mu} = \gamma \cdot \boldsymbol{P} \tag{1.11}$$

γ is called magnetogyric ratio which is a constant for every existing isotope and furthermore also an indicator for the sensitivity of the nucleus (large γ, high sensitivity). The angular momentum $\mathbf{P}$ is similar to electromagnetic waves a quantized dimension, which has its origin in the rotation of the nucleus about its own axis. It is defined in Eq. 1.12.

$$\boldsymbol{P} = \sqrt{I(I+1)}\ \hbar \tag{1.12}$$

I, the angular momentum quantum number, can adopt values ranging from 0, $\frac{1}{2}$, 1.. up to 6. By combining Eq. 1.11 and 1.12 one yields Eq. 1.13.

$$\boldsymbol{\mu} = \gamma\ \sqrt{I(I+1)}\ \hbar \tag{1.13}$$

By looking at this equation, it gets obvious that only nuclei with a non-zero angular momentum ($\mathrm{I} \neq 0$) posses a magnetic moment and therefore can be detected via NMR.

If a nucleus is positioned in an external static magnetic field, the component $\mathrm{P_Z}$ of the angular momentum orientates itself in the same direction as the external field. It orientates in such a manner that Eq. 1.14 becomes valid.

$$\boldsymbol{P_Z} = m \cdot \hbar \tag{1.14}$$

The magnetic quantum number m can take 2I+1 different values, which is the same amount like the values of the angular momentum $\mathbf{P_Z}$. This characteristic is named directional quantization and is illustrated in Fig. 1.7 a.

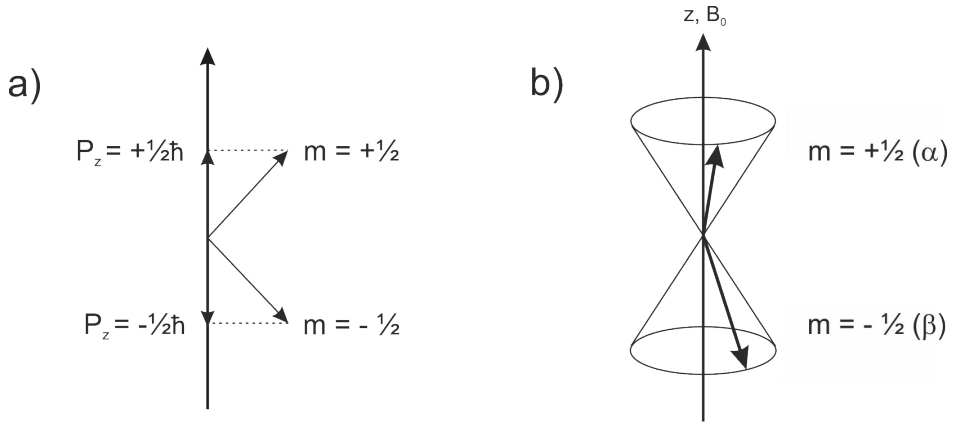

Fig. 1.7: a) Illustration of the directional quantization of **P** of a nucleus with I = $\frac{1}{2}$.
b) Precession of the nuclear dipols about the z-axis.
Adapted from reference[15]

The nuclear dipoles are precessing about the z-axis with a certain precession frequency ω_{L}, called Lamor frequency, which is defined by Eq. 1.15.

$$\omega_{\mathrm{L}} = |\frac{\gamma}{2\pi}|B_0 \tag{1.15}$$

The precession around the z-axis is shown in Fig. 1.7 b).

A nuclei with an angular momentum quantum number of I = $\frac{1}{2}$, as for example ^{19}F, has not only two possible orientations, but also two energy states. These possible energy states are called Zeeman levels and their energy and the difference between the two energy levels is given in Eq. 1.16 and Eq. 1.17.

$$E = m\gamma\hbar B_0 \tag{1.16}$$

$$\Delta E = \gamma\hbar B_0 \tag{1.17}$$

The population of these energy states ($\frac{N\alpha}{N\beta}$) follows a Boltzmann statistic as given in Eq. 1.18.

$$\frac{N_\beta}{N_\alpha} = exp(-\frac{\Delta E}{k_B T}) = 1 - \frac{\gamma\hbar B_0}{k_B T} \tag{1.18}$$

Normally the difference between the energy states is extremely small and only few flipping events (transition between the energy states) occur. As a consequence, the population of the energy levels is almost equal and furthermore out of Eq. 1.17 it can also be reasoned that the energy difference gets larger with increasing magnetic field B_0. To induce flipping, energy has to be applied, for example in the form of an radio-

frequency pulse in a way that Eq. 1.19 is valid.

$$\Delta E = h \cdot \nu \tag{1.19}$$

As the population of the lower energy state (N_α) is generally lower, absorption of energy is the event to occur more likely. This energy absorption gives then rise to the actual signal, if the resonance condition 1.20 is valid.

$$\omega_L = \nu_1 = |\frac{\gamma}{2\pi}| \cdot B_0 \tag{1.20}$$

The Eq. above shows that the frequency is different for every nucleus and magnetic field.

NMR experiment and introduction of the vector model based on the longitudinal relaxation

In the course of a NMR experiment a radio-frequency pulse with a fixed frequency, adapted to the nuclei and the magnetic field, is emitted and excites for instance all ^{19}F-nuclei at once. This pulse, with an energy of several watts typically, irradiates the sample for a couple of μs.

The magnetic vector of the rf-pulse, applied along the x-axis, interacts with the macroscopic magnetization M_0. To be more specific only the component (B_1) of the magnetic field of the rf-pulse, which rotates in the same way as the nuclear dipoles, is able to interact with M_0. M_0 is tipped away from its original axis x' (rotating coordination system), which is also the direction of B_0, by B_1 into the y', z plane. The angle of tipping Θ is depended on γ, the amplitude of B_1 and the pulse length, as stated in Eq. 1.21.

$$\Theta = \gamma \cdot B_{1i} \cdot \tau_P \tag{1.21}$$

In NMR experiments 90 ° and 180 ° pulses are most common. The transverse magnetization $M_{y'}$, which is detected by the receiver coil in the duration of the NMR experiment, is at maximum if a 90 ° pulse is applied. In contrast to that, the magnetization $M_{y'}$ becomes zero in the case of a 180 ° pulse. This fact gets important, if it comes to the determination of the right pulse length τ_P previous to the NMR experiment, in order to guarantee the greatest signal amplitude.

After the irradiation of the nucleus with a rf-pulse, M_0 is precessing about the z-axis. In the course of the relaxation M_z becomes M_0 again, whereas $M_{x,\,y}$ go to zero.

The decay of the $M_{y'}$, the transverse magnetization, is detected as free induction decay (FID) and gives the signal after the Fourier Transformation (FT).

The course of M_z with time gives the longitudinal relaxation (spin-lattice relaxation) as described by Eq. 1.22 and the relaxation time is denoted by T_1.

$$\frac{dM_z}{dt} = -\frac{M_z - M_o}{T_1} \tag{1.22}$$

1.4.1 MAS NMR

In the field of solid-state NMR not only relaxation processes can be detected, but it is also possible to determine the number of places of a certain kind of nuclei in a sample with MAS NMR. The spectrum is recorded in high-resolution and therefore more information is accessible.

In liquids there is no orientational dependence of magnetic effects due to the fast motion of the molecules, resulting in narrow lines in the NMR spectra. In contrast to liquids, solid molecules are not able to perform a sufficient rapid motion, yielding broad lines. This orientational dependence can be eliminated with Magic Angle Spinning NMR (MAS NMR), where the sample is rotated at high frequencies of up to kHz at an angle of 54.74 ° with respect to B_0. The orientational dependence can be either obliterated completely or partially, resulting in spinning sidebands in the later case.[30]

1.5 Polarisation Measurement

The electrical conductivity of all synthesised F^--ion conductors was determined via polarisation measurement. The practicle principle was first reported in 1952 by Hebb M. H.[22]. The determination of the electric conductivity relies on the principle that the ionic current through the sample is inhibited by using a blocking electrode like Au or Pt. Usually a non-blocking electrode is used at the other side of the sample, eg. Ag if the electrical conductivity of AgBr is to be determined[16].

The measurements conducted in the course of this thesis were carried out in a different set-up. On both sides ion blocking electrodes made of Au were used, which are permeable for electrons, but not for F^--ions. A set potential is then applied whereas ion gradients form, letting the current drop to a steady state after some time. The time to reach a steady state is dependent on the charge carrier mobility in the sample. A sharp decay of current is observable in materials with high mobility. At the steady state, charge transfer across the sample occurs only due to the electronic conductivity of the sample and after the steady state current is identified, the electrical conductivity σ_{El} is calculated[41] with Eq. 1.23.

$$\sigma_{\mathrm{El}} = \frac{I}{U} \cdot \frac{d}{r^2 \cdot \pi} \tag{1.23}$$

where

σ_{El} : electrical conductivity [$\mathrm{S\,cm^{-1}}$]
I : current at steady state [A]
U : polarisation voltage [V]
d : thickness of the pellet [cm]
r : radius of the pellet [cm]

1.6 Fluoride Ion Batteries

In 1976 a basic principle of a working galvanic cell based on F^--ions as charge carrier was first reported in literature by Kennedy et al.[23] and Schooman et al.[37].

Then until 2011 hardly any research was done in the field of rechargeable batteries based on fluorine, when M. Reddy and M. Fichtner[33] published the first experimental proof of a reversible working cell. Such FIBs are being researched, because they offer certain advantages compared to other systems; a theoretical energy density of $5000\,\mathrm{WhL^{-1}}$ and high theoretical potentials are possible[34][33].

In the first reversible working cell, metallic Ce was used as anode and a mixture of BiF_3, carbon and the used electrolyte $La_{0.9}Ba_{0.1}F_{2.9}$ as cathode. Below, the half cell reactions as well as the overall cell reaction are listed, for discharging of the system described above.

$$\begin{array}{rccc} \text{Cathode:} & \mathrm{x\,e^-} + \mathrm{MF_x} & \rightarrow & \mathrm{M} + \mathrm{x\,F^-} \\ \text{Anode:} & \mathrm{x\,F^-} + \mathrm{M'} & \rightarrow & \mathrm{M'F_x} + \mathrm{x\,e^-} \\ \hline \text{Cell:} & \mathrm{MF_x} + \mathrm{M'} & \rightarrow & \mathrm{M'F_x} + \mathrm{M} \end{array}$$

In this first approach of building a FIB, all three layers (anode, cathode and electrolyte) were pressed together, with a relatively high electrolyte thickness of approximately 700 μm. The resulting pellets were tested in Swagelok type cells at a temperature of 150 °C, to ensure sufficient conductivity of the electrolyte. Up to 38 cycles were obtained with an initial capacity of $190\,\mathrm{mAh\,g^{-1}}$ (theoretical value: $302\,\mathrm{mAh\,g^{-1}}$) and a final capacity of approximately $50\,\mathrm{mAh\,g^{-1}}$. Despite this comparatively high number of possible cycles, the capacity fades quickly.

In further publications other electrode combinations in the charged as well as in the discharged state were examined. Nevertheless it must be mentioned that all these cells which could be cycled suffer from severe capacity fading and do not reach theoretical capacity values. An overview of several cells is shown in Table 1.1 on page 16.

It must be noted that all cells with solid state electrolytes were measured at elevated temperature (150 °C) to ensure a sufficient high conductivity of the electrolyte[33][34][35]. To lower the temperature, a different approach using a fluoride doped PEG-matrix with several solvents was done, as liquid electrolytes offer a high conductivity at ambient temperatures. Although it was feasable to run the cell at ambient temperatures, again no cycling was possible[19].

Even though the interest in FIBs was slowly emerging in the last years, still a lot of research is necessary, concerning not only the active materials, but also the electrolyte and the fabrication, to reach acceptable capacities as well as cycling behaviour.

1.7 Galvanostatic cycling with potential limitation (GCPL)

To investigate the charging and discharging characteristic of a battery, the cells are subjected to GCPL. In the course of this experimental investigation, negative or positive constant current is applied. The most important information derived from GCPL is the dis-/charging capacity, which is plotted against the cycle number, to detect the capacity fade over time[27].

1.8 Cyclic Voltammetry (CV)

CV is a widespread method to investigate redox reactions, which can occur in various systems, for example electrochemical stability in batteries.

In principle, the potential is ramped with time at a certain scan rate [V/s] in a defined potential window and the current is recorded. Therefore a three-electrode set-up is usually used. In a single-sweep experiment the voltage starts from the initial potential (e.g. OCV) and is reversed, as soon as the vertex potential (e.g.$-3\,\mathrm{V}$) is reached. It is again reversed at the second vertex potential (e.g. $2\,\mathrm{V}$) and ends at the final potential (e.g. again the initial OCV). If the voltage circulates several times and possibly also at different scan rates, one speaks of a multi-sweep experiment. With rising scan rate the recorded current increases too, whereat a positive current marks the region of oxidation reactions, a negative current the region of reduction reactions. A CV can provide a large variety of informations, including occurring redox reactions and reversibility.[27][21]

Table 1.1: Overview of several different FIBs reported in literature.

Anode	**Cathode**	**Electrolyte**	**Potential [V]**	**Capacity [mAh g^{-1}]**	**Further remarks**
Ce	CuF_2/C	$La_{0.9}Ba_{0.1}F_{2.9}$	2.88	322 (61 %)	discharged with 10 μA cm^{-1} at 150 °C no cycling reported[33]
—"—	BiF_3/C Solid Solution	—"—	2.15	190 (62 %)	discharged with 10 μA cm^{-1} at 150 °C **50 mAh g^{-1} after 38 cycles**[33]
—"—	BiF_3/C Composite	—"—	2.61	126 (42 %)	discharged with 10 μA cm^{-1} at 150 °C no cycling reported[33]
Al/C	CoF_3, FeF_3, CuF_2, BiF_3	—"—	0.2 - 0.3	-	only "tiny" capacities[20]
CeF_3/C	Bi	$La_{0.9}Ba_{0.1}F_{2.9}$	0.1 - 0.4	404 (theor.: 385)	at 150 °C side reactions ($\beta - BiF_{3-2x}O_x$, BiF_5) only 2 cycles[34]
Mg + Mg_2/C	—"—	—"—	~1.8	266 (69 %)	at 150 °C 50 cycles to below 50 mAh g^{-1}[34]
Mg + MgF_2	Cu	—"—	~1.8	390	cycling at 150 °C 10 cycles possible to a discharge capacity below 20 mAh g^{-1}[34]
Li	BiF_3	$Ba_{0.6}La_{0.4}F_{2.4}$	~2.8	110	two cycles possible[35]

2 Experimental Section

2.1 Synthesis of F^--ion Conductors

The mechanochemical synthesis of the F^--ion conductors $La_{0.9}Ba_{0.1}F_{2.9}$, $BaSnF_4$ and $RbSn_2F_5$ was carried out with over night in vacuum dried stochiometric amounts of the respective reactants (SnF_2 - Sigma Aldrich 99 %, RbF - Sigma Aldrich 99.8 %, BaF_2 - chempur 99.9 %, LaF_3 - alfa aesar 99.99 % (REO)) in a high energy planetary mill (Fritsch Pulverisette 7 premium line). To conduct the synthesis, ZrO_2 grinding beaker with a volume of 45 ml were used, as well as 180 balls made out of ZrO_2 with a diameter of 5 mm, with a final ball to powder ration of 18:1. The educts were milled for 10 h at 600 rpm, whereas a break of 15 min was taken after every 15 min to allow cooling of the beakers. The charging as well as the discharging of the beakers was done in a glovebox under Argon atmosphere (O_2 and $H_2O < 0.5$ ppm) to avoid any contamination.

$La_{0.9}Ba_{0.1}F_{2.9}$ was further used without annealing, all other compounds were subject to a subsequent annealing step, described in subsection 2.1.1 and 2.1.2.

2.1.1 Annealing of $RbSn_2F_5$

As previous annealing of the milled, powdery compound lead to no success, the powders were pressed with a force of 0.5 tons for 2 minutes to pellets with a diameter of 5 mm and a weight of 100 mg, to ensure sufficient contact between the particles. The annealing step was either carried out under constant Ar flow or the pellets were melt into a vial under vacuum to provide an oxygen and moisture free atmosphere. The annealing took place in a tube furnace for different time periods at several temperatures. The results with corresponding annealing time and temperature are presented in section 3.2.

2.1.2 Annealing of $BaSnF_4$

The annealing of $BaSnF_4$ in powdery form was carried out in a tube furnace under constant Ar flow at 300, 315 and 330 °C for 2 h in order to reach the complete transformation of cubic to layered tetragonal $BaSnF_4$.

2.2 Electrochemical Impedance Spectroscopy (EIS)

For impedance spectroscopy 60 - 80 mg of the particular powder was pressed to pellets with a diameter of 5 mm at a pressure of 0.5 t for 2 minutes. To ensure sufficient electrical contact between pellet and electrode, a 100 nm thick Au layer was sputtered onto both sides of the pellets with a LEICA EM SCD050 sputter machine regulated by a LEICA EMQSG100 control system.

The measurement was conducted with a broadband impedance spectrometer (Novocontrol Concept 80), in combination with a BDS 1200 cell and a ZGS cell interface. Frequencies covered a range starting from 10^{-2} Hz up to 10^{7} Hz. The temperature was controlled with a QUATRO Cryosystem and varied between -120°C and 200°C. The whole measurement was conducted under constant, dry N_2 atmosphere.

2.3 X-ray Diffraction (XRD)

The synthesised samples were characterized using XRD under atmospheric pressure and room temperature. A Bruker D8 Advance Diffractometer with Bragg Brentano geometry and Cu K-α radiation was used, whereat points were taken from 10 until 100° 2Θ with an interval of 0.02° 2Θ measured one second each. The Rietveld Refinement was carried out with X-PertHighScorePlus (PANalytical).

2.4 Simultaneous Thermal Analysis (STA)

A STA of unannealed $RbSn_2F_5$ was conducted with a Netzsch STA 409 dynamic calorimeter. To avoid contamination, the used Pt crucible was filled under Argon atmosphere in a glovebox (O_2 and $H_2O < 0.5$ ppm). The sample was heated with a heating rate of 30 K/min from 298 K to 593 K.

2.5 Light Microscopy and Scanning Electron Microscopy (SEM)

The surface of $RbSn_2F_5$ which was annealed as pellet at 295, 265 and 225 °C, was investigated with a Olympus BX60 light microscope.

In order to get deeper insight into the deposited structures on the surfaces, SEM was performed with a VEGA3 TESCAN electron microscope. Furthermore EDX was done to determine the chemical composition qualitatively and quantitatively.

2.6 NMR

Relaxation time measurements

The relaxation times T_1 as well as $T_{1\rho}$ of $La_{0.9}Ba_{0.1}F_{2.9}$ and $RbSn_2F_5$ were determined using a Bruker Avance III 300 NMR spectrometer with a magnetic field of 7.04 T, resulting in a resonance frequency of 281.79 MHz for a ^{19}F nuclei. A custom built NMR probe for ^{19}F was used.

MAS NMR

^{19}F, ^{119}Sn as well as ^{87}Rb MAS NMR measurements were carried out on a Bruker Avance III 500 spectrometer with a magnetic field of 11.7 T, resulting in a resonance frequency of 186.40 MHz for ^{119}Sn nuclei, 470.30 MHz for ^{19}F nuclei and 163.60 MHz for ^{87}Rb nuclei. The spectra were recorded by rotating 2.5 mm rotors with a frequency of 25 kHz at a temperature of 30°C in the MAS probe head PH MASDVT500WB BL2.5. As the rotation generates heat, the actual rotor temperature is typically higher. The target gas flow was set to 400 lph, the frame cooling to 35 %. Following references were used: ^{119}Sn - SnO_2 (−604.3 ppm), ^{19}F - LiF (−204.3 ppm), ^{87}Rb - $RbNO_3$ (−30 ppm, site 3).

2.7 Polarisation measurement

In order to conduct the DC polarisation measurement of all F^--ion conductors, the powders were pressed to pellets with a diameter of 8 mm and an height of approximately 1 mm at a pressure of 0.5 t for 2 minutes. To guarantee electrical contact between pellet and electrode, a 100 nm thick Au electrode was sputtered on both pellet sides with a LEICA EM SCD050 sputter machine regulated by a LEICA EMQSG100 control system.

The pellets were mounted into a cell as pictured on the next page in Fig. 2.1, which was continuously purged with N_2 and connected to a Parstat MC potentiostat (Princeton Applied Research) equipped with a low-current option. The electrical conductivity of $BaSnF_4$ and $La_{0.9}Ba_{0.1}F_{2.9}$ was determined at a temperature of 200°C, whereas $RbSn_2F_5$ was only heated up to 120°C in order to prevent crystal growth, which was assumed to occur at higher temperatures during the measurement. The measurement was conducted three times each, with potentials of 0.2 V, 1.5 V and 3 V.

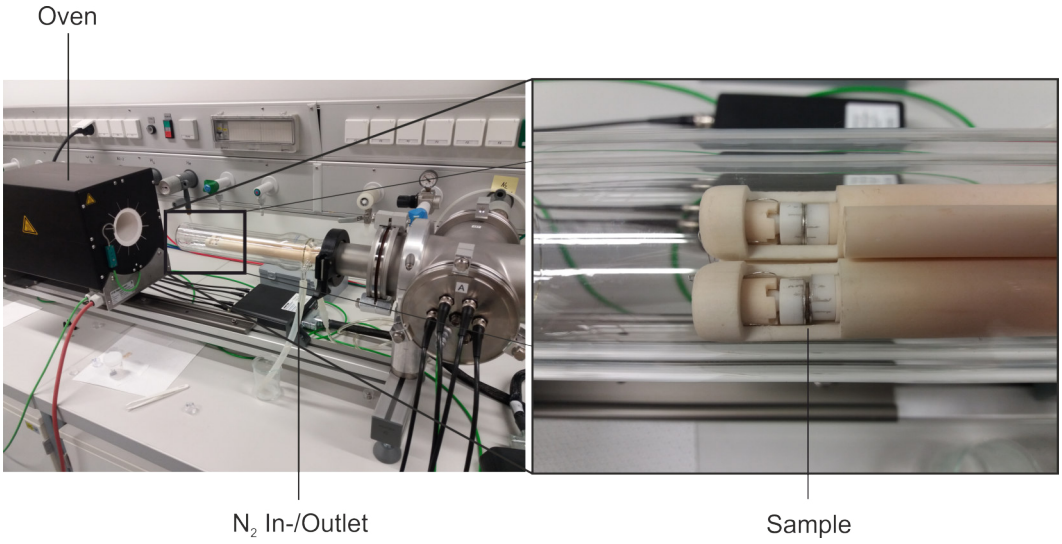

Fig. 2.1: Set-up for the polarisation measurement.

2.8 Assembly of the cells

With each solid-state electrolyte ($BaSnF_4$, $La_{0.9}Ba_{0.1}F_{2.9}$ and $RbSn_2F_5$) two different cathode-anode compositions were subjected to GCPL. These compositions are stated in Table 2.1.

Table 2.1: Overview of anodes and cathodes used

Stage	**Anode**	**Cathode**
Charged	Li foil	BiF_3 / C65 / electrolyte (30 wt% / 10 wt% / 60 wt%)
Discharged	LiF / C65 / electrolyte (30 wt% / 10 wt% / 60 wt%)	Bi / C65 / electrolyte (30 wt% / 10 wt% / 60 wt%)

The production of all cathodes and the LiF-anode was carried out in a high-energy planetary mill (Fritsch Puverisette 7 premium line) by milling at first appropriate amounts of the active material with C65 at 600 rpm for 10 h in tungsten carbide beakers with a volume of 45 ml and 170 tungsten carbide balls with a diameter of 5 mm. Subsequently the electrolyte was added and the whole mixture was again milled for 10 h at 150 rpm. This procedure was based on a similar one reported in literature[33]. The charging as well as the discharging of the beakers was done in a glovebox under Argon atmosphere (O_2 and $H_2O < 0.5$ ppm) to avoid any contamination.

In order to obtain stable pellets and good interfacial contact of all layers, the bulk-type approach was choosen[33]. This approach is based on the principle that a relatively thick layer of electrolyte is pressed densely together with cathode, anode and current collectors.

For visualisation a schematic build-up is presented in Fig. 2.2 and 2.3.

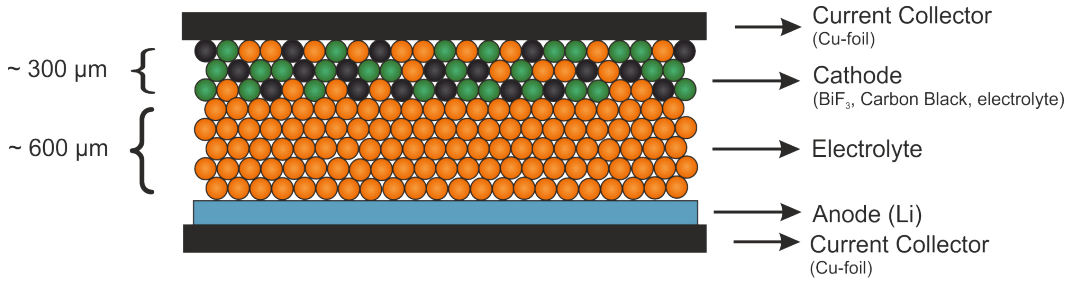

Fig. 2.2: Schematic build-up of the FIB assembly in the charged state, adapted from reference[40].

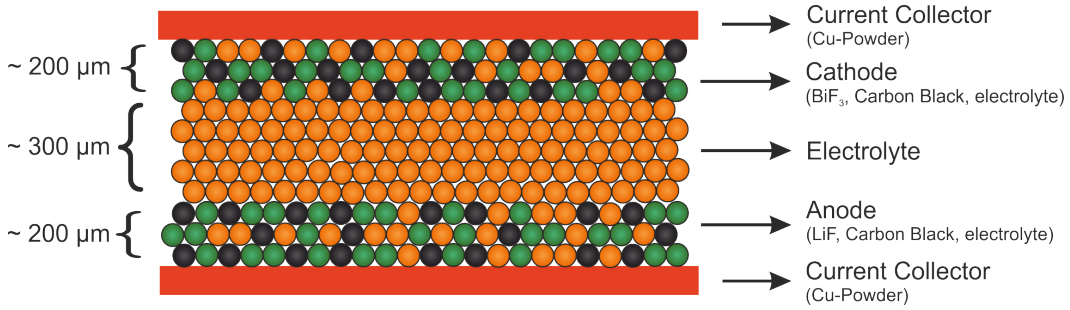

Fig. 2.3: Schematic build-up of the FIB assembly in the discharged state.

In a 8 mm die at first an appropriate amount of electrolyte was compressed with 0.3 t. The corresponding weight and thickness of all electrolytes used are listed in Table 4.1 in the appendix. Subsequently the cathode as well as a Cu foil, acting as current collector, were pressed to the electrolyte with 0.5 t. In the end Li foil and again Cu foil were placed at the other side of the electrolyte and pressed just slightly.

In the case of the cells assembled in the discharged state, all components were powdery and therefore pressed layer by layer only by squeezing the die with hands. The whole pellet was finally pressed with 0.5 t. Powdery Cu was used as current collector on both sides, because the stability of the pellet was increased drastically by doing so.

Finally the pellets were assembled in a Swagelok type two electrode cell and put into an oven operated at 120°C.

2.9 GCPL

The cells were subjected to GCPL using a multichannel VMP-3 or MPG-2 potentiostat from Biologic Science Instruments operated by the EC Lab Software. Therefore a counter, connected to a reference electrode, and a working electrode were connected to the anode and cathode side, respectively. The GCPL was carried out in a voltage range from 0.1 V to 3 V with currents of $\pm 12\,\mu$A, $\pm 24\,\mu$A, $\pm 48\,\mu$A and $\pm 96\,\mu$A.

2.10 Cyclic Voltammetry (CV)

CV was carried out with $RbSn_2F_5$, $BaSnF_4$ and $La_{0.9}Ba_{0.1}F_{2.9}$. Therefore the powders were pressed to pellets with a diameter of 8 mm and an height of approximately 1 mm at a pressure of 0.5 t for 2 minutes. To guarantee electrical contact between pellet and electrode, a 100 nm thick Au working electrode was sputtered on one complete pellet side with a LEICA EM SCD050 sputter machine regulated by a LEICA EMQSG100 control system. On the other pellet side a 100 nm thick Au counter electrode with a diameter of 2 mm was sputtered.

The pellets were mounted into the same cell used for the polarisation measurement, connected to a Parstat MC potentiostat (Princeton Applied Research) equipped with a low-current option. The whole cell was heated to 200°C in the case of $BaSnF_4$ and $La_{0.9}Ba_{0.1}F_{2.9}$, and to 120°C in the case of $RbSn_2F_5$. As the oven induced stray currents in the measuring lines that disturbed the measurement, it was switched off for the relatively short durance of the measurement, resulting in slightly fluctuating temperatures.

The initial potential was set to the corresponding OCV value, the vertex potential to -3 V and the final potential again to OCV. The scan rate was increased from 0.1 to 1 V/s after two cycles each.

As the CV was carried out without the use of a reference electrode, which is needed to control the potential accurately, the CVs might not be quantitatively precise and should be interpreted in a qualitative manner.

3 Results and Discussion

3.1 $La_{0.9}Ba_{0.1}F_{2.9}$

3.1.1 XRD

In Fig. 3.1 the diffractogram of $La_{0.9}Ba_{0.1}F_{2.9}$ is shown. Even though the reflexes are broadened due to the disorder and amorphous content of the material, the reflexes correspond well with the reference, which is indicated by vertical bars. The reflexes are also identical with the ones of LaF_3 with a slight difference in the lattice parameters. The lattice parameters of $La_{0.9}Ba_{0.1}F_{2.9}$ ($a = b = 7.224\,\dot{A}$, $c = 7.39\,\dot{A}$) are slightly higher than the ones of LaF_3 ($a = b = 7.16\,\dot{A}$, $c = 7.36\,\dot{A}$) reported in literature (ICSD: 27089), which indicates that the lattice structure remained the same, but with a slight lattice disortion due to the larger, incorporated Ba^{2+} on La^{3+} places.

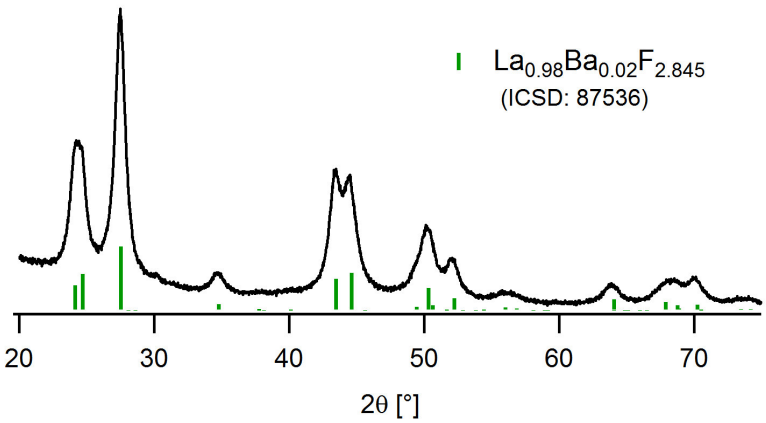

Fig. 3.1: Diffractogram of $La_{0.9}Ba_{0.1}F_{2.9}$

3.1.2 Impedance Spectroscopy

The synthesised $La_{0.9}Ba_{0.1}F_{2.9}$ was further characterised by impedance spectroscopy. The conductivity isothermes, which were recorded in a temperature range from −120 °C to 200 °C, are plotted in Fig. 3.2 a). The sample features a conductivity of $9.67 \cdot 10^{-5}$ S·cm^{-1} at 160 °C which coincides well with the values reported in literature[33] ($2.8 \cdot 10^{-4}$ S·cm^{-1} at 160 °C).

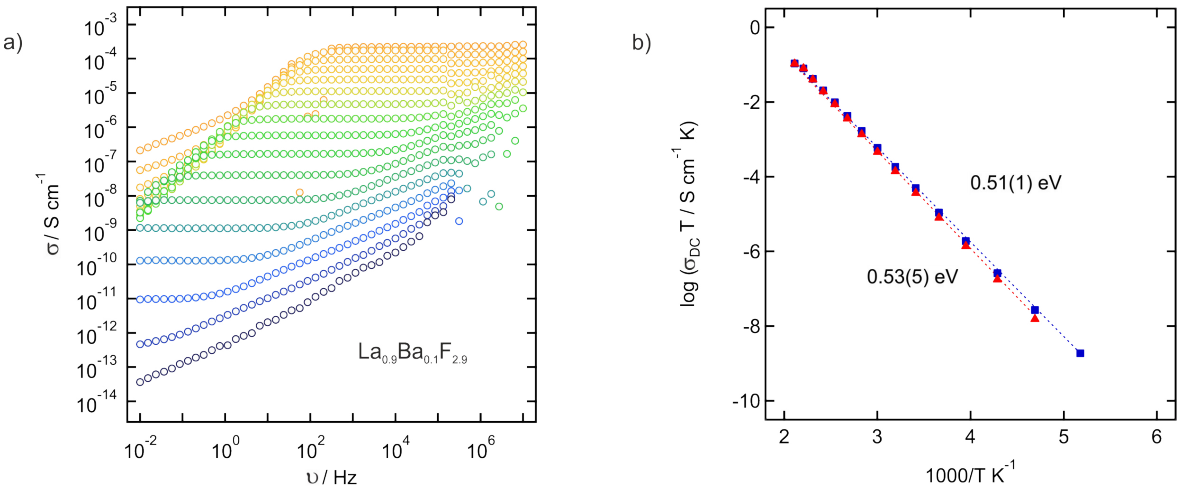

Fig. 3.2: Impedance Spectroscopy of $La_{0.9}Ba_{0.1}F_{2.9}$
a) Conductivity isothermes recorded from 200 °C to −120 °C in a frequency range between 10^{-2} and 10^{7} Hz
b) Arrhenius Plot for the cooling (in blue) and heating run (in red)

The corresponding Arrhenius plot was constructed to calculate the activation energy and is shown in Fig. 3.2 b). The activation energy differs slightly for heating and cooling run, with values of 0.53(5) eV and 0.51(1) eV. In literature[36] an activation energy of 0.55 eV is reported which is also in good accordance with the presented data.

3.1.3 Polarisation Measurement

The results of the DC polarisation of $La_{0.9}Ba_{0.1}F_{2.9}$, which was carried out at potentials of 0.2 V, 1.5 V and 3 V, is shown in Fig. 3.3.

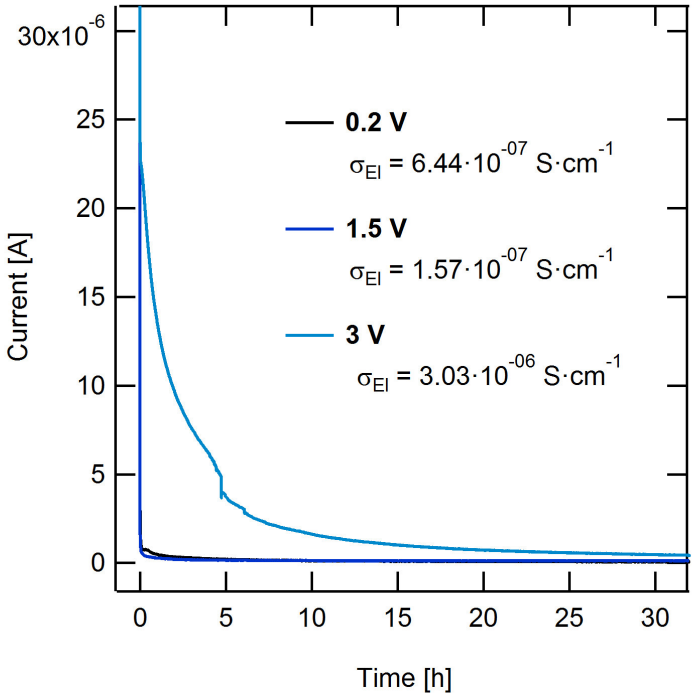

Fig. 3.3: DC polarisation measurement of $La_{0.9}Ba_{0.1}F_{2.9}$ at 200 °C, carried out at potentials of 0.2, 1.5 and 3 V.

A steady-state current is reached within a short time period (<5 h), when the polarisation is carried out with 0.2 and 1.5 V. In this two cases, the decay of current in the beginning of the experiment is similar and very steep, indicating a good overall conduction in the material at this temperature. In contrast it takes much longer (>30 h) to reach a steady-state current, if the sample is being polarised with a potential of 3 V. As shown in Fig. 3.3 the electrical conductivity rises significantly with increasing potential. This might have its origin in the fact, that more charge carriers move due to migration rather than diffusion, which might be dominant at lower potentials. Another possible explanation might be that at relatively high potentials (3 V) the compound is no longer electrochemically stable. Thus, the slow decay of the current at 3 V could be caused by a electrochemical reaction rather than just the build-up of a concentration gradient at the electrodes. The electrochemical degradation of the material might also account for the slight increase of the electron transport.

The overall conductivity of $La_{0.9}Ba_{0.1}F_{2.9}$ determined by impedance spectroscopy is $2.27{\cdot}10^{-4}\,S{\cdot}cm^{-1}$ at 200 °C. The electrical conductivity is therefore two to three orders of magnitude lower than the ionic one, which is calculated by subtracting the electrical from the overall conductivity

3.1.4 Cyclic Voltammetry

Fig. 3.4 shows the CVs of $La_{0.9}Ba_{0.1}F_{2.9}$ recorded at a temperature of 195 °C ± 4 °C and scanning rates between 0.1 V and 1 V/s.

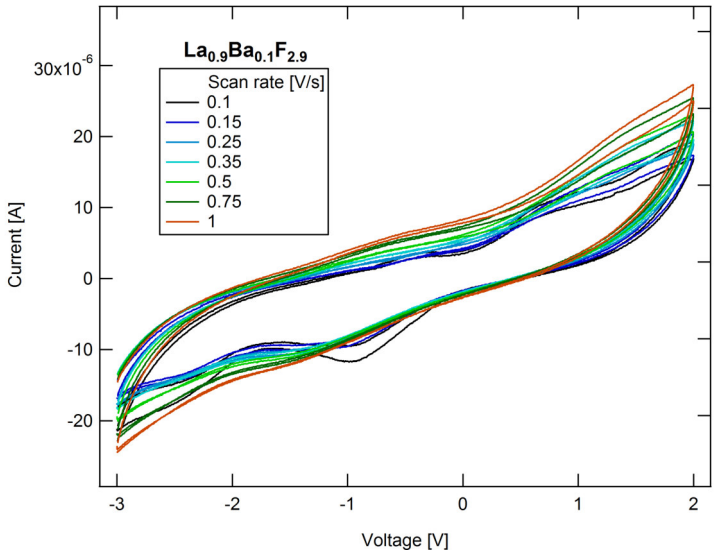

Fig. 3.4: CV of $La_{0.9}Ba_{0.1}F_{2.9}$ at scanning rates between 0.1 and 1 V/s recorded at a temperature of 195 °C ± 4 °C

It is not obvious, whether a redox reaction occurs or not, as the curves are not showing clear current peaks. However, the overall shape of the curves is changing only slightly when increasing the scan rate, indicating reversible processes. With respect to that, $La_{0.9}Ba_{0.1}F_{2.9}$ is a suitable solid state electrolyte at elevated temperatures.

3.1.5 NMR

^{19}F - MAS NMR

Fig. 3.5 is showing the ^{19}F MAS NMR spectrum of $La_{0.9}Ba_{0.1}F_{2.9}$ recorded at a temperature of 30 °C.

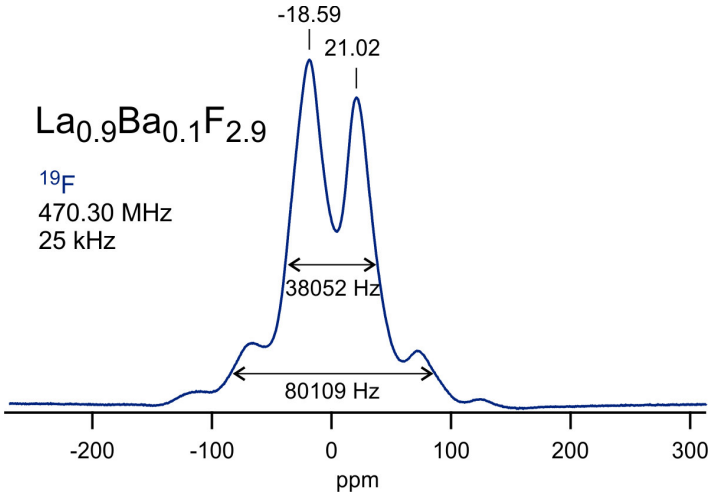

Fig. 3.5: ^{19}F MAS NMR spectra of $La_{0.9}Ba_{0.1}F_{2.9}$ (with 40 ppm = 18.8 kHz)

Two main lines at −18.59 ppm and 21.02 ppm are present, which could not be separated completely. Additionally satellites occur, being the 25 kHz and 50 kHz spinning sidebands. According to literature[36] (^{19}F MAS, 338 MHz, spinning speed of 40 kHz) the line at 21.02 ppm is assigned to the positions F2+3, the line at −18.59 ppm to position F1 in $La_{0.9}Ba_{0.1}F_{2.9}$. As the position F2 and F3 are nearly equivalent, the lines coincide.

T_1 and $T_{1\rho}$ - NMR

Relaxation measurements were carried out to determine T_1 and $T_{1\rho}$ of the synthesised $La_{0.9}Ba_{0.1}F_{2.9}$. The obtained Arrhenius plot, in which the inverse temperature K^{-1} is plotted against $\log(\frac{1}{T_1,1\rho})$, is presented in Fig. 3.6.

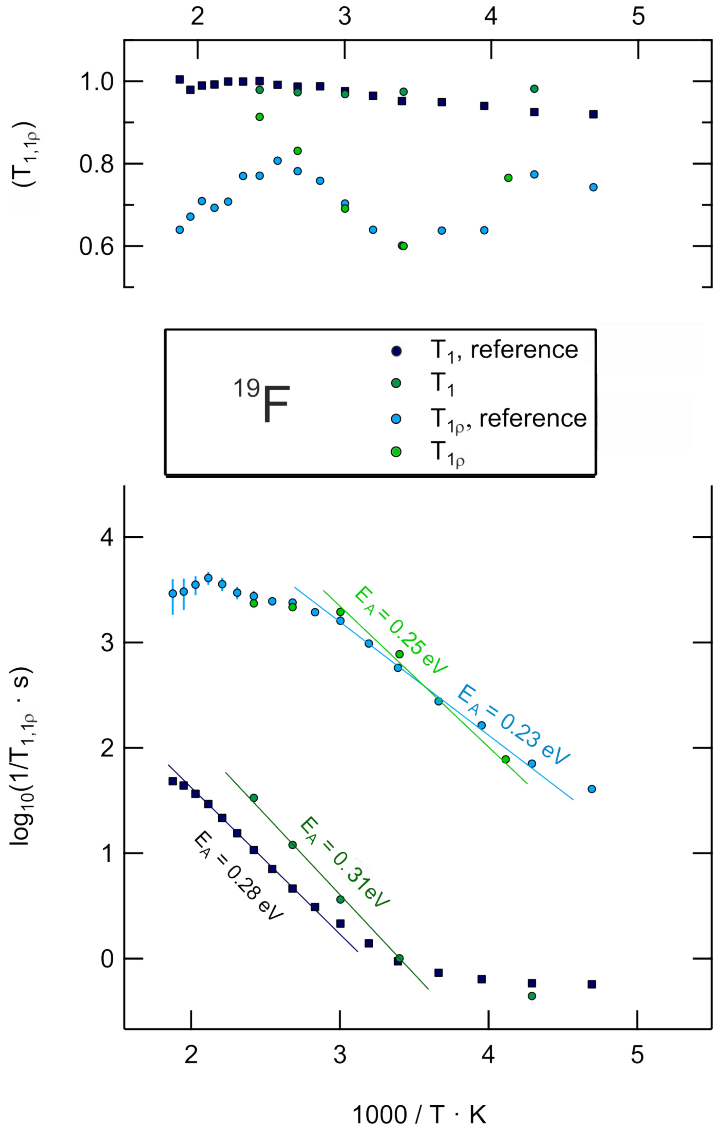

Fig. 3.6: Arrhenius plot of T_1 and $T_{1\rho}$ of $La_{0.9}Ba_{0.1}F_{2.9}$

In addition to the values of the self synthesised sample, the values of a reference sample[1] obtained over a larger temperature range are illustrated for comparison. The values of both $T_{1\rho}$ times coincide well and the slopes $(-\frac{E_A}{k_B T})$ of the fitted curves in the linear region give similar activation energies of 0.25 eV and 0.23 eV (reference). These values are as expected considerably lower than the activation energy of 0.51 eV

[1]Sample synthesised and measured by DI S. Breuer

determined by impedance spectroscopy. This is due to the fact that local motions are detected via NMR, whereas long range diffusion plays the crucial role in impedance measurements, resulting in a higher activation energy. The self synthesised sample yields a slightly higher activation energy of 0.31 eV in the case of T_1 measurements, compared to the reference (0.28 eV).

In this case it was not possible to calculate the correlation time and the jumping rate, as none of the curves are showing clear maxima, especially in the case of $T_{1\rho}$ times, as the values at higher temperatures fluctuate. Measurements at higher temperatures would be needed here.

3.2 $RbSn_2F_5$

3.2.1 STA

Before several annealing steps were performed, STA was carried out to detect eventual occurring phase transformations. At low temperatures the signal was subjected to strong fluctuations and is therefore not meaningful. Only two rather small exothermic peaks could be determined at onset temperatures of 184 °C and 208 °C and a decomposition temperature of approximately 300 °C, as it is represented in Fig. 3.7.

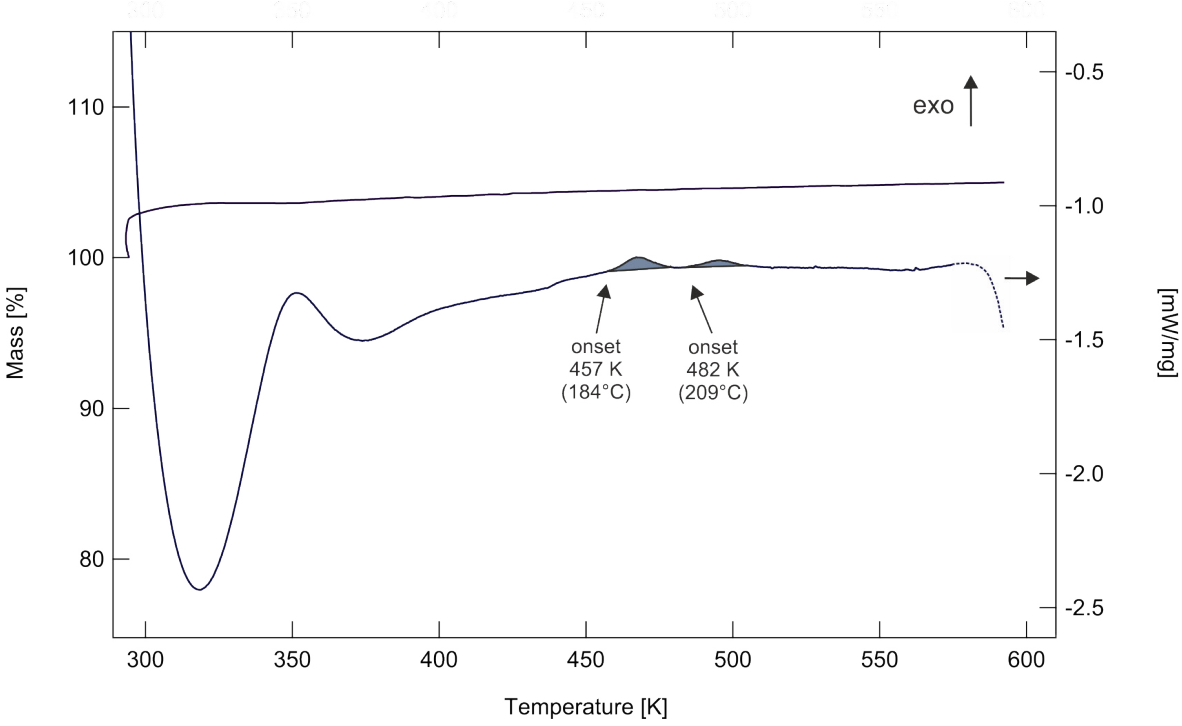

Fig. 3.7: STA of $RbSn_2F_2$ carried out with a heating rate of 30 K/min between 300 and 600 K.

For this reason the first three annealing steps were carried out at 295 °C, 265 °C and 225 °C, to assert that all eventually occurring phase transformations take place. On the surface of the pellet, which was annealed at 295 °C, dark blue metallic precipitates were observed, which decreased in size when lowering the annealing temperature.

Due to the formation of this precipitates the annealing temperature was then further lowered to 200 °C, 150 °C and 100 °C.

3.2.2 Light and Electron Microscopy

The precipitates formed on the surface of the pellets, annealed at 295 °C, 265 °C and 225 °C, were further explored via light and electron microscopy. The 40-fold magnification obtained by light microscopy of $RbSn_2F_5$ annealed at 295 °C is pictured in Fig. 3.8. The pellet exhibited a very rough surface, covered by metallic and white crystals.

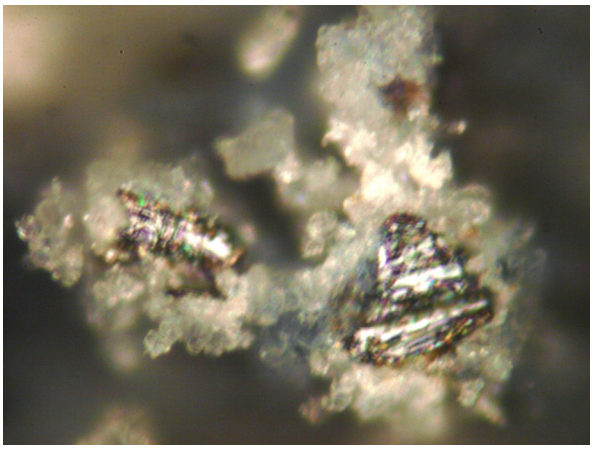

Fig. 3.8: $RbSn_2F_5$ annealed at 295 °C, picture obtained via light microscopy under 40 fold magnification.

$RbSn_2F_5$ annealed at 265 °C presented crystallites on the surface too. Pictures obtained by light as well as SEM are shown in Fig. 3.9. Compared to $RbSn_2F_5$ annealed at 295 °C, smaller and more elongated crystals are present on the surface. To get an insight in the composition of these crystals, EDX was carried out (see Appendix, Fig. 4.3). The EDX result would suggest that the shiny crystallites are most probably composed of metallic tin, which was on contrary not found in XRD or ^{119}Sn-MAS NMR measurements and is therefore unlikely present in the sample.

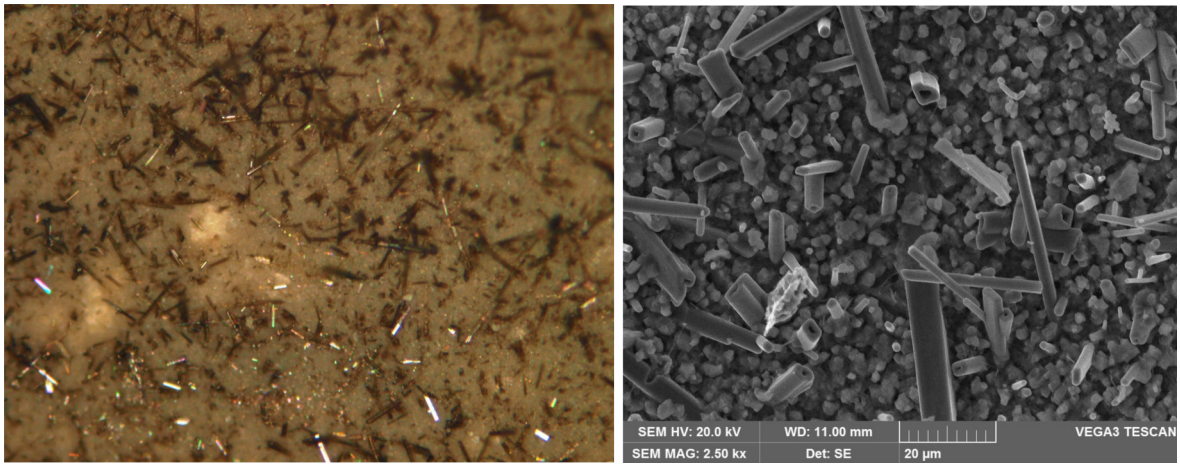

Fig. 3.9: $RbSn_2F_5$ annealed at 265 °C
left: Picture obtained via light microscopy under 20 fold magnification
right: SEM picture under 2500 fold magnification

As pictured in Fig. 3.10, $RbSn_2F_5$ annealed at 225 °C showed even smaller precipitates. At lower annealing temperatures no crystal growth on the surface could be observed.

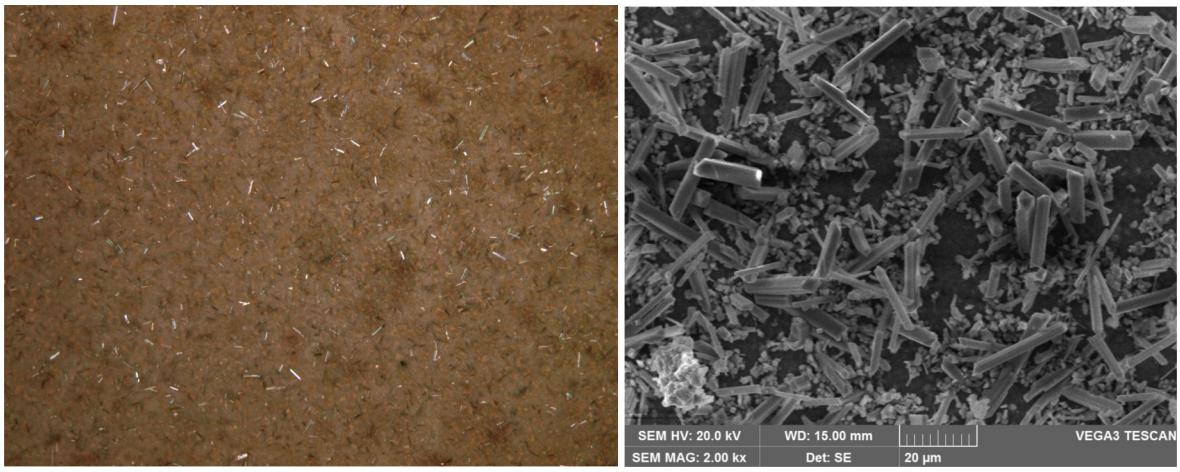

Fig. 3.10: $RbSn_2F_5$ annealed at 225 °C
left: Picture obtained via light microscopy under 20 fold magnification.
right: SEM picture under 2000 fold magnification.

3.2.3 XRD

In Fig. 3.11 the diffractograms of all annealed samples of $RbSn_2F_5$ are shown.

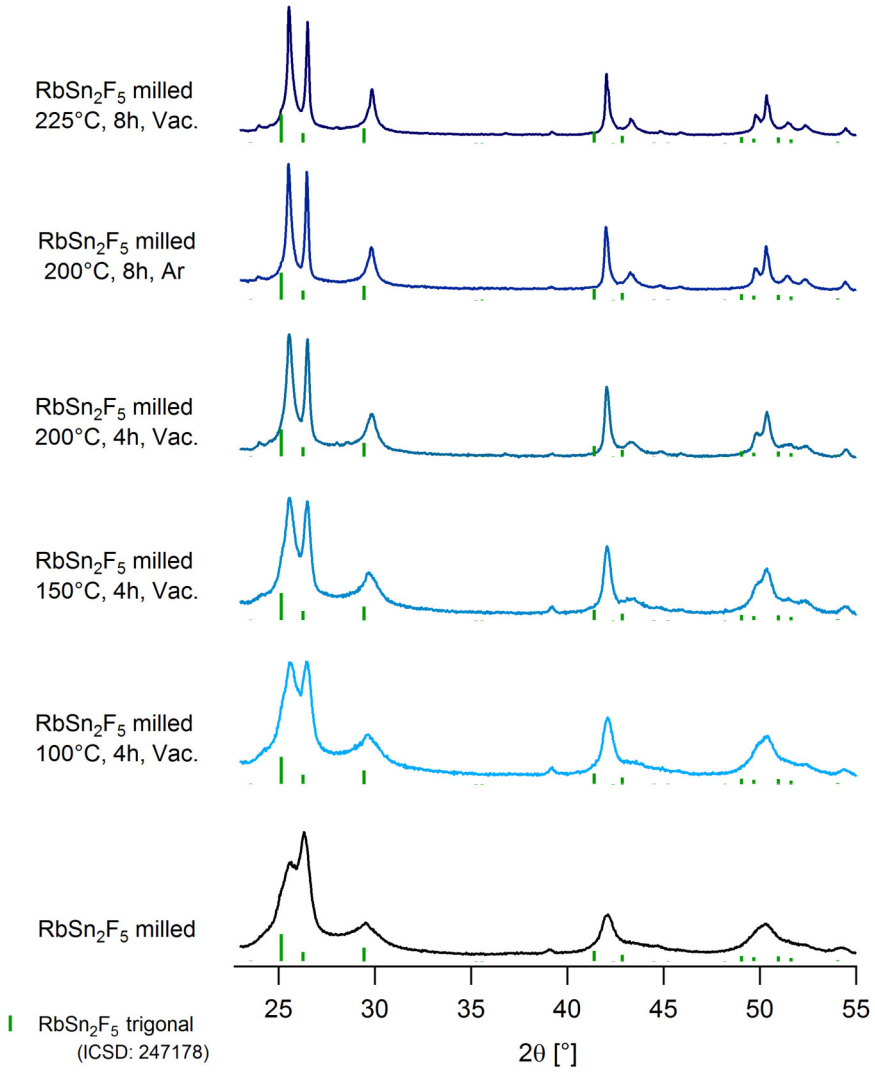

Fig. 3.11: XRD diffractograms of $RbSn_2F_5$

At first it has to be noted that the reflections get narrower, if the samples are annealed longer and/or at higher temperatures, as expected due to the crystal growth. Contrary to the STA which indicated a phase change at 184 °C and 209 °C, the phase remained unvaried within all samples. Furthermore all reflections are shifted to slightly higher values of $2°\theta$ compared to the reference, which is indicated by vertical bars. In literature[39] it was proven by in-situ XRD that there is a shift of reflections when the temperature is increased. This fact points out that a reversible change occurs, which can not be detected by XRD at room temperature.

3.2.4 Impedance Spectroscopy

The conductivity of $RbSn_2F_5$, annealed at 200 °C for 8 hours, was measured via impedance spectroscopy at various frequencies between −100 °C and 200 °C. The obtained conductivity isothermes are plotted in Fig. 3.12 a).

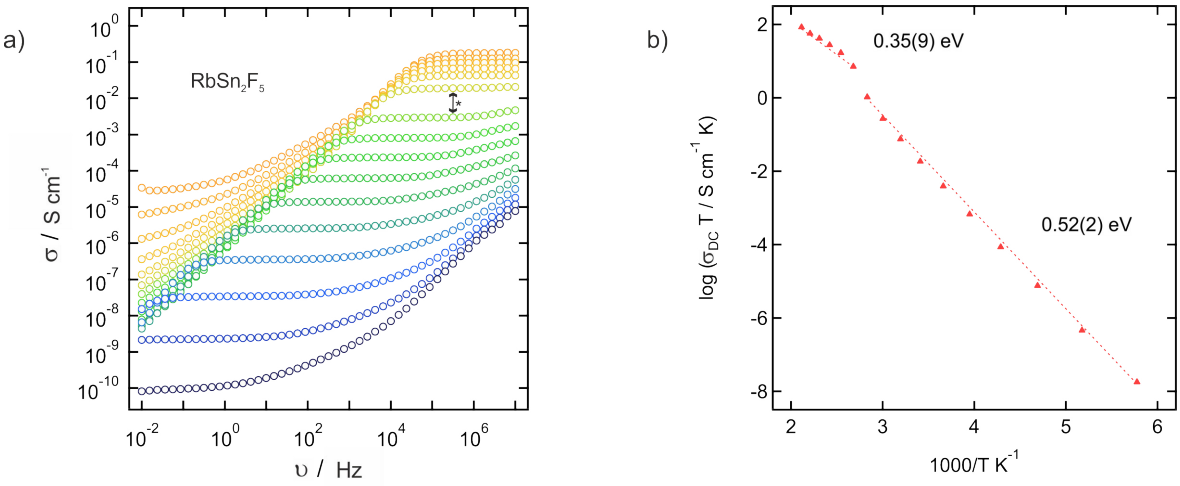

Fig. 3.12: Impedance spectroscopy of $RbSn_2F_5$
a) Conductivity Isothermes recorded from 200 °C to −120 °C in a frequency range between 10^{-2} and 10^{7} Hz
b) Arrhenius Plot of the cooling run

The σ_{DC}-plateaus are visible for every temperature measured and shift, as expected due to the higher mobility of the ions, to higher frequencies with increasing temperature. Between the isothermes at a temperature of 80 °C and 100 °C respectively, the ionic conductivity is increasing disproportionately, highlighted with a *, which corresponds to the transformation to the superionic phase. The conductivity reaches a value of $6.32{\cdot}10^{-5}\,S{\cdot}cm^{-1}$ at 20 °C and $0.125\,S{\cdot}cm^{-1}$ at 180 °C. Compared to literature[2] ($0.113\,S{\cdot}cm^{-1}$ at 180 °C) the values are slightly higher, which might have its origin in the mechanochemical synthesis, compared to a hydrothermal synthesis in literature.

In order to calculate the activation energy, the Arrhenius plot was constructed and is presented in Fig. 3.12 b). It shows two regions easy to distinguish. The activation energy above 100 °C is 0.36 eV, whereas it rises to 0.52 eV at lower temperatures. This observation is in agreement with the detected increase of conductivity at this temperature. Compared to literature (0.45 eV / 0.55 eV)[2] the activation energy is lower, as expected due to the higher conductivity.

3.2.5 Polarisation Measurement

The result of the DC polarisation of $RbSn_2F_5$, which was carried out at potentials of 0.2 V, 1.5 V and 3 V, is shown in Fig. 3.13 along with the calculated electrical conductivity σ_{El}.

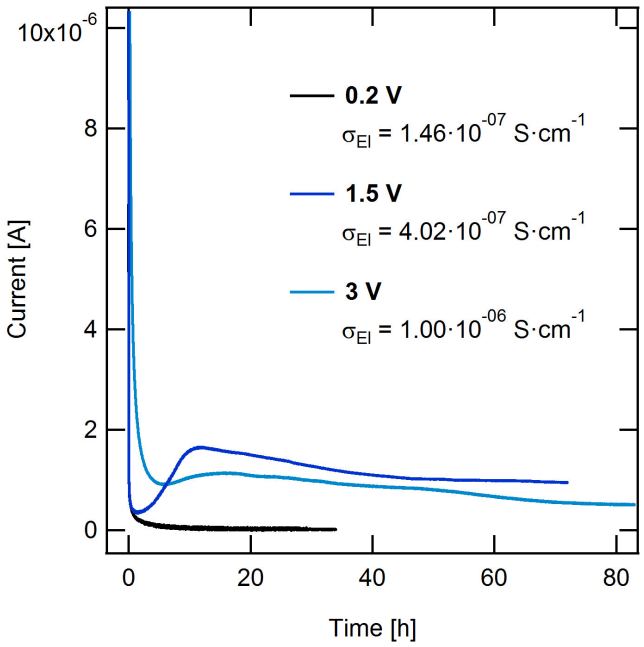

Fig. 3.13: DC polarisation of $RbSn_2F_5$ carried out at 120 °C and at potentials of 0.2, 1.5 and 3 V

When the sample is being polarised with a potential of 1.5 V it takes approximately 20 hours to reach a steady state current, whereas it takes already 80 hours in the case of 3 V. Again the electrical conductivity σ_{El} of $RbSn_2F_5$ increases with rising potential and is compared to the ionic conductivity at this temperature (0.043 $S \cdot cm^{-1}$) comparatively small. Attention has to be paid on the course of the current of the polarisation curves measured at a potential of 1.5 and 3 V. Here the current decreases to a certain minimum value, before increasing especially at 1.5 V steep until approximately 11 hours. This is not seen when the sample is polarised at 0.2 V and it may indicate a reaction or decomposition of the sample at higher voltages. The electrochemical degradation of the material could also be accompanied by an increase of the electronic conductivity. It must be noted, that the Au electrode on one pellet side changed the colour from gold to silver after the measurement, suggesting a reaction too. These observations are in good agreement with the monitored fluctuations of the OCV, when $RbSn_2F_5$ is employed as solid state electrolyte in FIBs (see Sec.3.4) and the CV results.

3.2.6 Cyclic Voltammetry

Fig. 3.14 shows the CV of $RbSn_2F_5$ recorded at a temperature of 115 °C ± 4 °C and a scanning rate of 0.1 V.

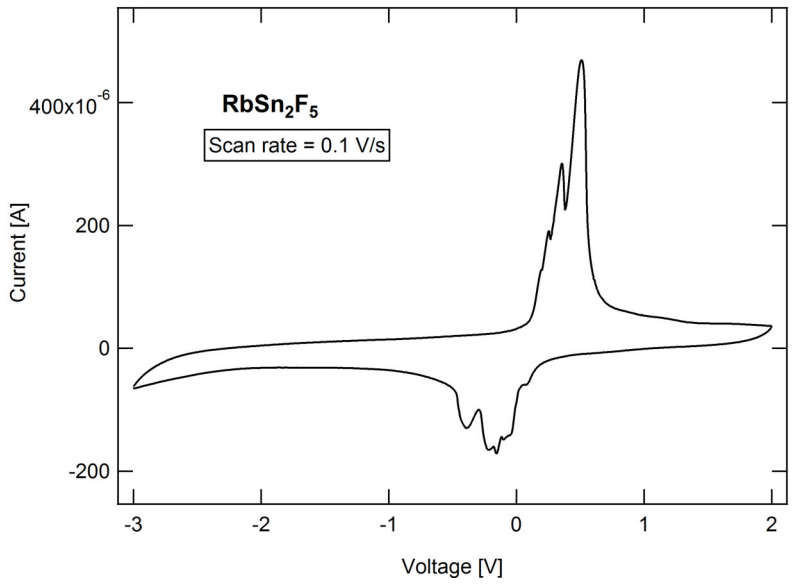

Fig. 3.14: CV of $RbSn_2F_5$ at a scanning rate of 0.1 V/s recorded at a temperature of 115 °C ± 4 °C

In the region of positive currents at 0.5 V two sharp peaks are present, denoting oxidation processes. Compared to these, the other peaks at negative currents are rather small, starting already at a potential of 0 V. Most probably Sn^{2+} is oxidised to Sn^{4+} during the anodic scan, while Sn^{2+} is finally reduced to Sn^0 during the cathodic scan.

Furthermore in Fig. 3.15 the CVs recorded at scanning rates between 0.1 and 1 V/s are illustrated.

If the sample is subjected to CV for a longer time and at higher scan rates, all peaks disappear, indicating a irreversible change in the sample. This observation is in good agreement with measurements of the OCV of $RbSn_2F_5$ assembled with Li and BiF_3 as FIB, before conducting GCPL. As $RbSn_2F_5$ is facing irreversible changes in this potential window, it is not the first choice as solid state electrolyte. In particular, we have to consider the small potential difference between the anodic peaks and the cathodic peaks. This is an indication of a very narrow electrochemical stability potential of this electroylte.

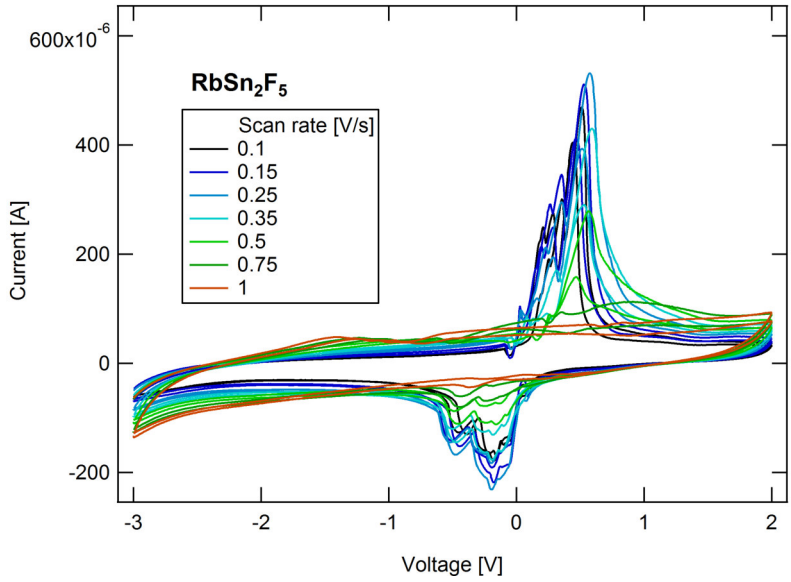

Fig. 3.15: CV of $RbSn_2F_5$ at scanning rates between 0.1 and 1 V/s recorded at a temperature of 115 °C ± 4 °C

SEM

To further investigate, whether Sn^0 develops finally, SEM was performed. The cross-section of one pellet, on which no CV was carried out, and of the pellet from the CV described prior, was examined using SE and BSE detectors. The corresponding pictures are shown in the appendix in Fig. 4.4.

The cross-section of the untreated pellet was polished with abrasive paper and is therefore showing a scratch on the surface. Beside that, both cross-sections offer a homogeneous surface. Additionally the pictures obtained with the BSE detector show no material contrast, indicating that Sn^0 has not formed. It could be that the relatively short time span, in which the CV was carried out, is not enough that large precipitates of Sn^0 form. Also, the voltage range might be too small. Here further experiments would be needed.

3.2.7 NMR

^{19}F - MAS NMR

The ^{19}F-MAS NMR spectrum of $RbSn_2F_5$ obtained at a temperature of 30 °C is shown in Fig. 3.16.

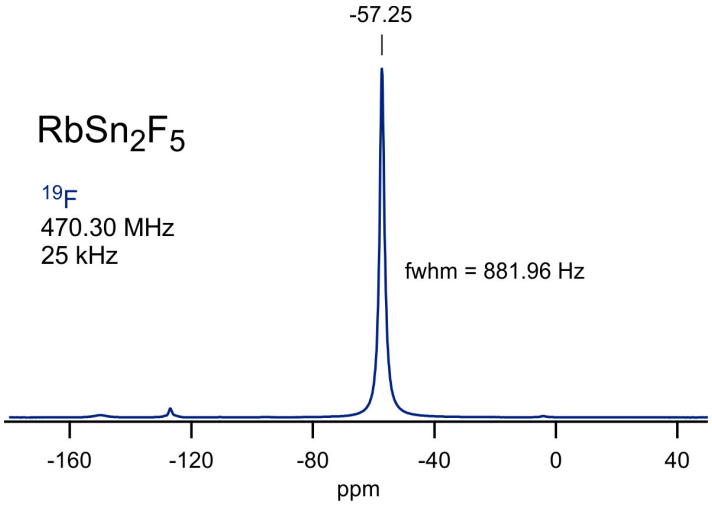

Fig. 3.16: ^{19}F-MAS NMR spectrum of $RbSn_2F_5$ (with 40 ppm = 18.8 kHz)

A central line is present at −57.25 ppm and a small signal at −126.91 ppm, which can be assigned to an impurity, eventually the starting material RbF, which is reported to have a similar chemical shift of −124 ppm (referenced to CCl_3F)[18]. As there are three different F^--ion positions in the structure of $RbSn_2F_5$ and only one line is present in the spectrum, all mobile F^--ions are facing the same chemical environment.

^{119}Sn - MAS NMR

In Fig. 3.17 the ^{119}Sn-MAS NMR spectrum of $RbSn_2F_5$ recorded at a temperature of 30 °C is shown.

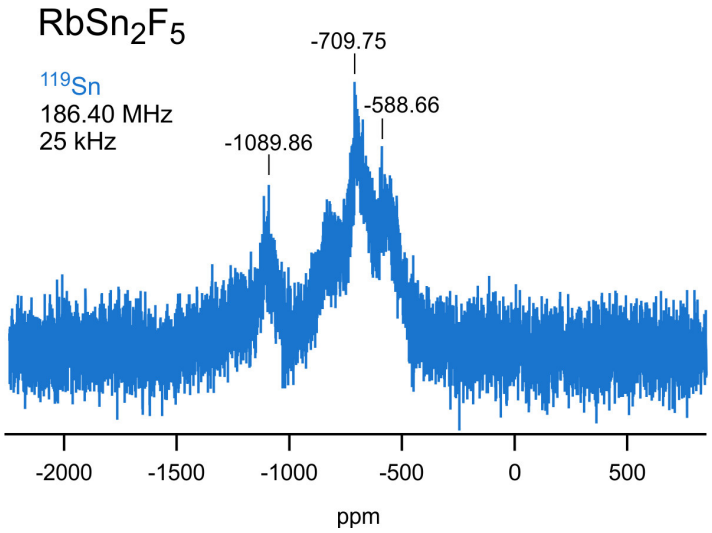

Fig. 3.17: ^{119}Sn-MAS NMR spectrum of $RbSn_2F_5$ (with 100 ppm = 18.6 kHz)

The signal-to-noise ratio (SNR) in this spectrum is low despite the experiment was carried out with a high number of scans, hence it is difficult to state how many Sn sites are present. Most probably the lines at −709.75 ppm and −1089.86 ppm are actual signals (eventual sidebands at −588.66 ppm and −831 ppm). This indicates two different Sn positions, contrary to the structure obtained by x-ray measurements showing that all Sn positions are equivalent.

^{87}Rb - MAS NMR

In Fig. 3.18 the ^{87}Rb-MAS NMR spectrum of $RbSn_2F_5$ measured at a temperature of 30 °C is illustrated.

In the spectrum one dominant line at 27.84 ppm is present, with another smaller one at −18.94 ppm, which is split up once again. This splitting occurs due to the electric interaction of the core ($I = \frac{5}{2}$) with the electrical field gradient. This indicates one position for Rb in $RbSn_2F_5$ coinciding with structure data obtained by x-ray diffraction.

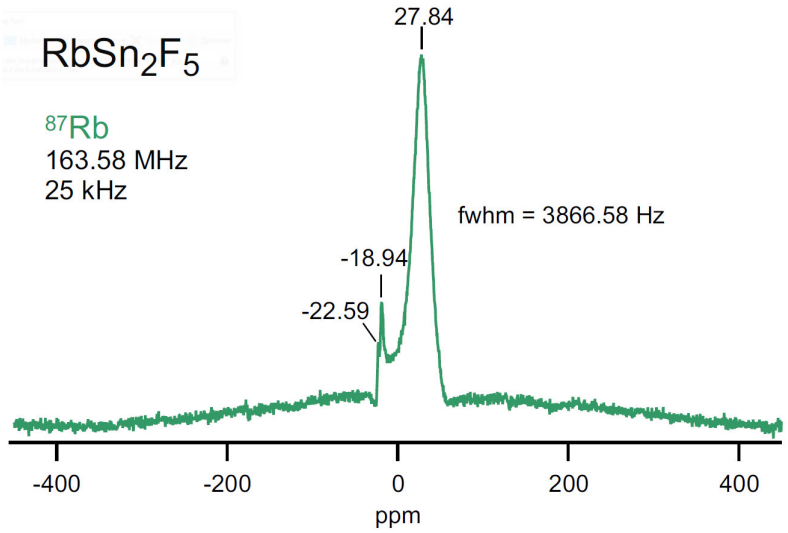

Fig. 3.18: ^{87}Rb-MAS NMR spectrum of $RbSn_2F_5$
(with 40 ppm = 6.5 kHz)

T_1 and $T_{1\rho}$ - NMR

^{19}F T_1 and $T_{1\rho}$ relaxation times of $RbSn_2F_5$ were recorded in a temperature range between 213 - 473 K and 213 - 353 K, respectively. In Fig. 3.19 the corresponding Arrhenius plot is illustrated.

In the Arrhenius plot the inverse temperature K^{-1} is plotted against the logarithm of $\frac{1}{T_1, T_1\rho}$. In the linear sections curves can be fitted, whose slopes $(-\frac{E_A}{k_B T})$ give the activation energies of the occurring diffusion processes.

In the case of T_1 only one flank is observable, giving an activation energy of 0.23 eV. This value coincides well with the activation energy of 0.24 eV of the $T_{1\rho}$ flank at lower temperatures. As the flanks of $T_{1\rho}$ are slightly asymmetric, the activation energy at higher temperatures reaches a value of 0.38 eV. These values obtained with relaxation measurements are, as expected, considerably lower than the ones gained through impedance measurement.

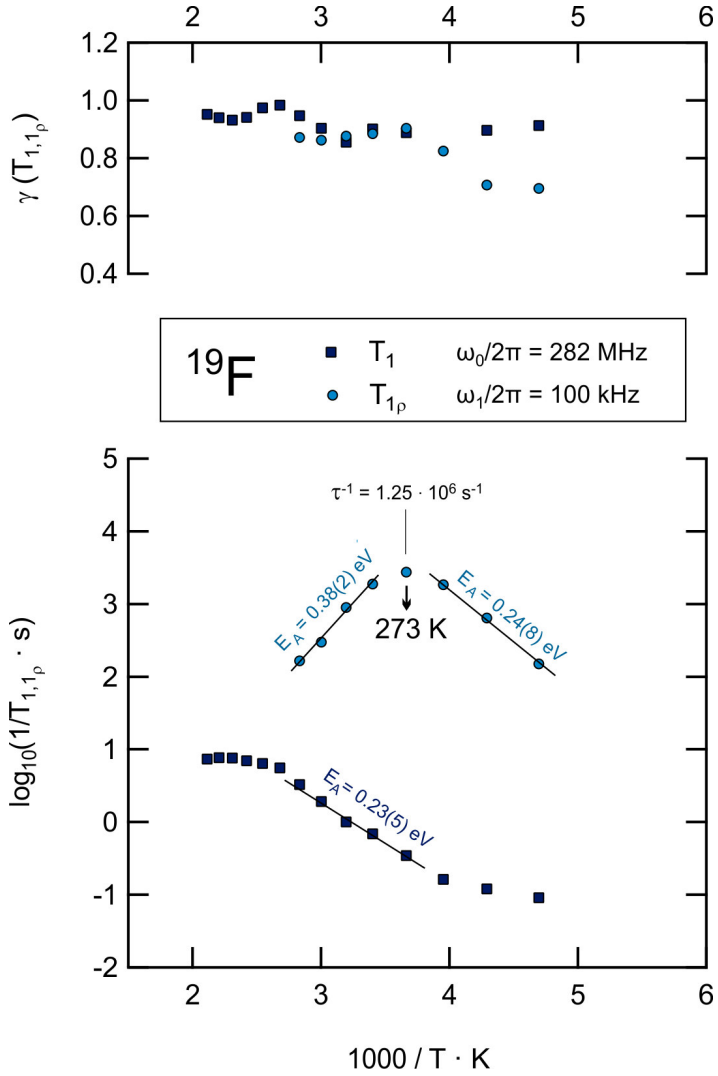

Fig. 3.19: Arrhenius plot of T_1 and $T_{1\rho}$ of $RbSn_2F_5$

A maximum value of $\log(1/T_1)$ is reached at a temperature of 273 K. The correlation time, which is related to the jump rate, was calculated with a spin-locking frequency of 100 kHz, Eq. 3.1 and 3.2.

$$\frac{\omega_1}{2\pi} = 100\,kHz \tag{3.1}$$

$$\omega_1 \cdot \tau = 0.5 \tag{3.2}$$

A correlation time τ of $7.98 \cdot 10^{-7}$ s and a jump rate τ^{-1} of $1.56 \cdot 10^6\,s^{-1}$ were determined.

3.3 $BaSnF_4$

3.3.1 XRD

In order to reach the highest content of tetragonal $BaSnF_4$ possible, annealing experiments were carried out at temperatures of 300, 315 and 330 °C. The respective diffractograms are shown in Fig. 3.20.

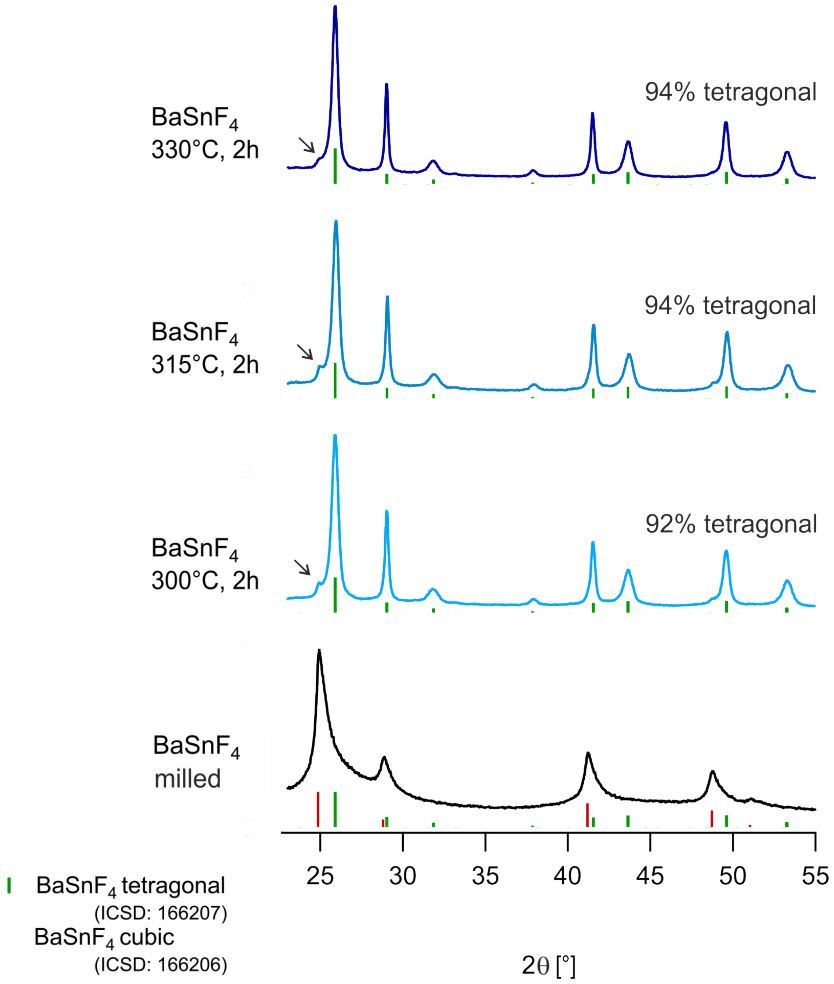

Fig. 3.20: XRD diffractograms of $BaSnF_4$

All annealed samples show a narrowing of the reflections due to the crystallite growth compared to the milled sample. The milled sample is already composed of a mixture of 49 % cubic and 51 % tetragonal $BaSnF_4$. It was possible to increase the tetragonal phase content to 94 % in the sample annealed at 330 °C for 2 hours. The remaining cubic content translates into a shoulder of the reflection at 26° 2Θ, indicated by an arrow in the diffractogram.

3.3.2 Impedance Spectroscopy

As the highest fraction of tetragonal $BaSnF_4$ was found to be present in the sample annealed at 330 °C for 2 hours, this sample was further subjected to impedance spectroscopy to determine the conductivity at temperatures ranging from − 100 °C to 200 °C. The obtained conductivity isothermes are illustrated in Fig. 3.21 a).

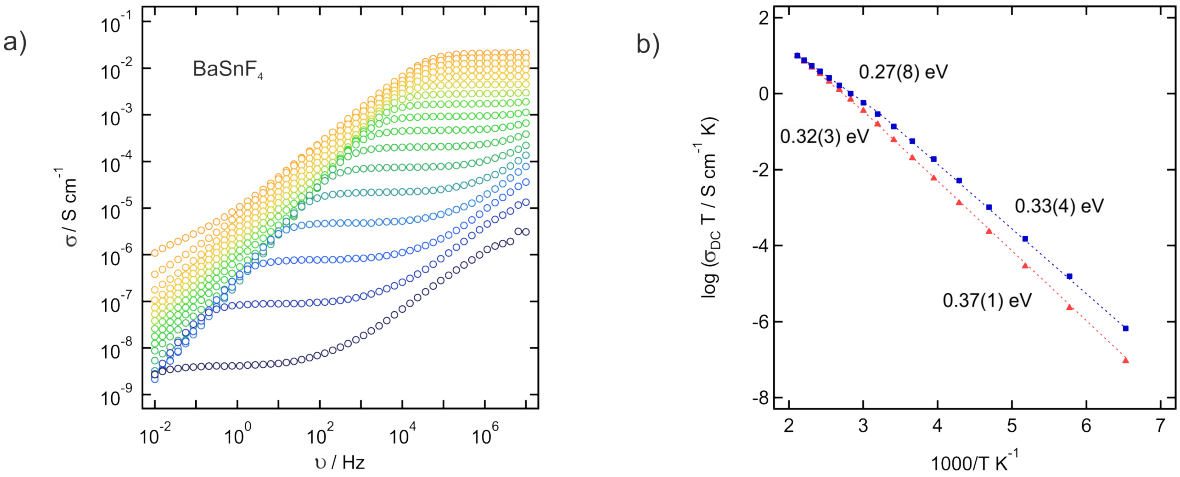

Fig. 3.21: Impedance spectroscopy of $BaSnF_4$ (330 °C, 2h)
a) Conductivity isothermes recorded from 200 °C to −120 °C in a frequency range between 10^{-2} and 10^7 Hz
b) Arrhenius Plot for the cooling (in blue) and heating run (in red)

A conductivity of $5.0{\cdot}10^{-4}$ S·cm^{-1} at 20 °C and $4.7{\cdot}10^{-3}$ S·cm^{-1} at 100 °C was reached. This values coincide with given ones in literature[28] ($3.2{\cdot}10^{-4}$ S·cm^{-1} at 100 °C).

Again, by reading off the values of DC-conductivity, an Arrhenius plot was created, which is shown in Fig. 3.21 b). The activation energy slightly differs for the data points recorded while heating and cooling the sample. Additionally both curves show two sections with different slopes, hence different activation energies, indicating a change in the material or conduction mechanism at approximately 60 °C.

3.3.3 Polarisation Measurement

The results of the polarisation measurement of $BaSnF_4$, carried out at potenials of 0.2, 1.5 and 3 V, is shown in Fig. 3.22.

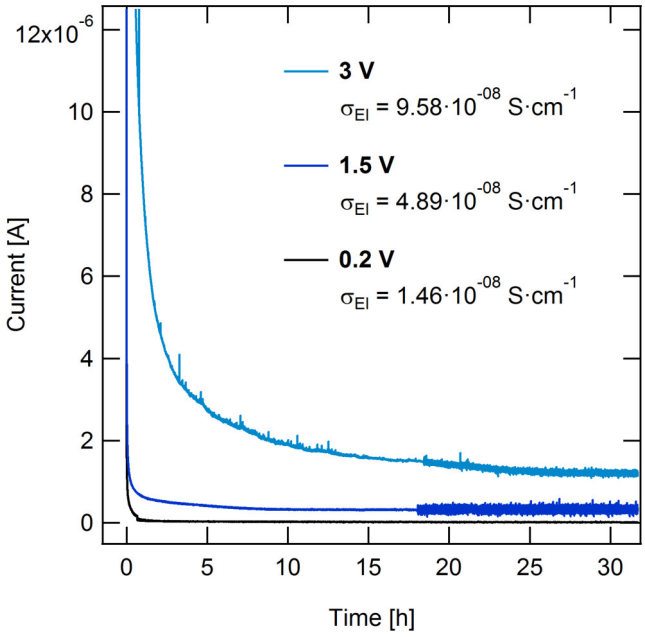

Fig. 3.22: DC polarisation of $BaSnF_4$ carried out at 200 °C and at potentials of 0.2, 1.5 and 3 V

Similar to $La_{0.9}Ba_{0.1}F_{2.9}$ a steady-state current is reached already in under 10 h in the case of 0.2 and 1.5 V, whereas it takes approximately 35 h to reach constant value when 3 V are applied. Also $BaSnF_4$ presents a higher electrical conductivity, when being polarised with a higher potential. An overview of the calculated electrical conductivities is given in Fig. 3.22.

Due to the comparatively low electrical conductivity the ionic conductivity is only insignificantly lower than the overall conductivity (0.02 $S \cdot cm^{-1}$) at this temperature.

3.3.4 Cyclic Voltammetry

Fig. 3.23 shows the CV of $BaSnF_4$ recorded at a temperature of $195\,°C \pm 4\,°C$ and a scanning rate of $0.1\,V/s$.

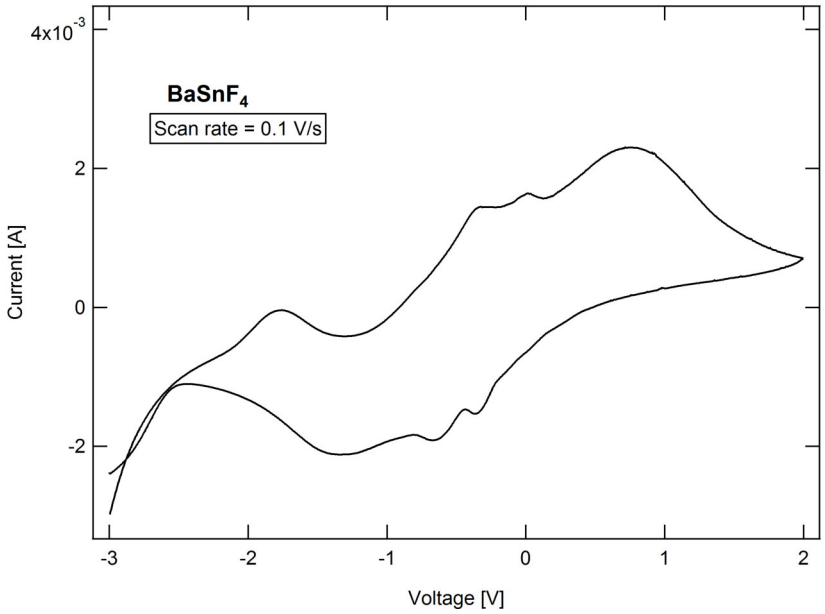

Fig. 3.23: CV of $BaSnF_4$ at a scanning rate of $0.1\,V/s$ recorded at a temperature of $195\,°C \pm 4\,°C$

This CV indicates that an oxidation as well as a reduction occurs, as peaks are present in both scan directions. Thereafter the scan rate was increased every 2 cycles up to $1\,V/s$ as presented in Fig. 3.24.

Starting with the CVs recorded at $0.15\,V$ no distinct reduction or oxidation peaks are present and the curves offer a nearly identical shape with increasing currents at higher scan rates.

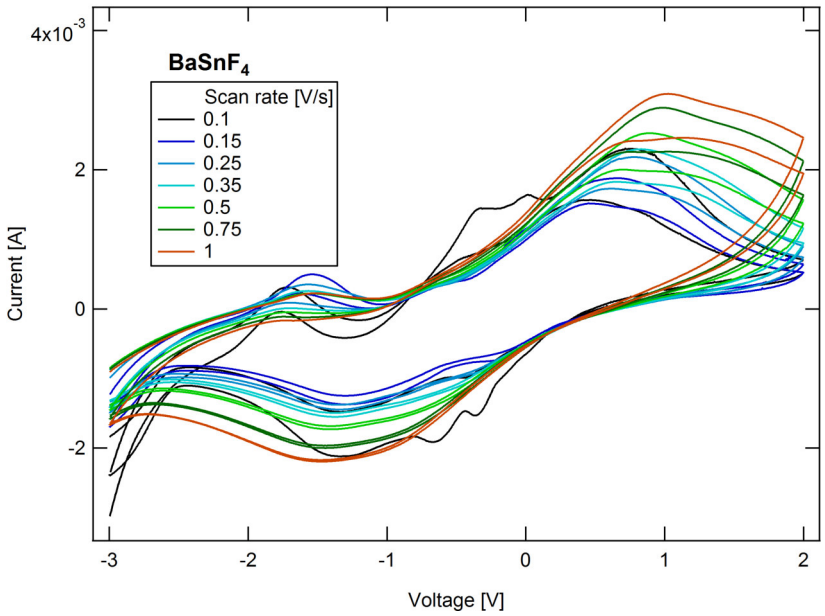

Fig. 3.24: CV of $BaSnF_4$ at scanning rates between 0.1 and 1 V/s recorded at a temperature of 195 °C ± 4 °C

3.3.5 NMR

^{19}F - MAS NMR

In Fig. 3.25 the ^{19}F-MAS NMR spectrum recorded at a temperature of 30 °C of $BaSnF_4$ is illustrated.

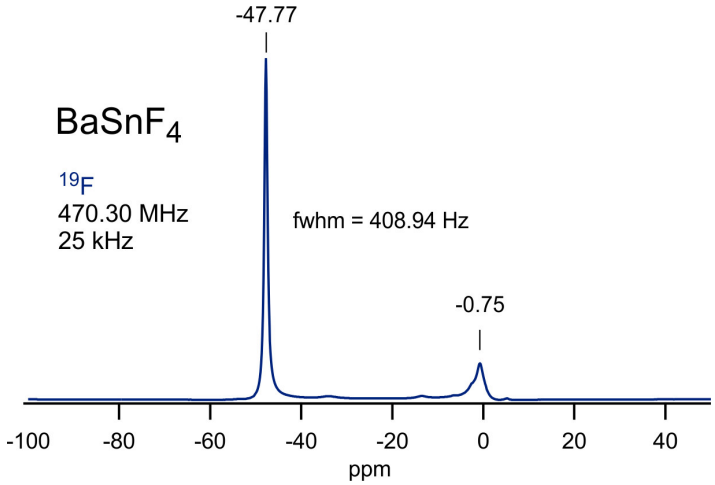

Fig. 3.25: ^{19}F-MAS NMR spectrum of $BaSnF_4$ (with 40 ppm = 18.8 kHz)

In the spectrum two rather narrow lines are visible at a chemical shift of −47.77 ppm and −0.75 ppm. This values coincide well with those presented in literature[9]. In literature the spectrum was acquired at a temperature of 35 °C, a spinning speed of 17 kHz and a resonance frequency of 338.75 MHz. With these parameters also two lines at a shift of −3 and −49 ppm and intensities similar to this spectra were obtained. The line at −49 ppm was assigned to F^--ions in SnF_2 environment, the line at −3 ppm to F^--ions in BaF_2 environment. With this information and the significant different intensities, it can be stated, that there are far more mobile F^--ions in the Ba-Sn layer than in the Ba-Ba layer. Thus the F^--ion conduction occurs mainly in the Ba-Sn-layer.

^{119}Sn - MAS NMR

The ^{119}Sn-MAS NMR spectrum of $BaSnF_4$ obtained at a temperature of 30 °C is illustrated in Fig. 3.26.

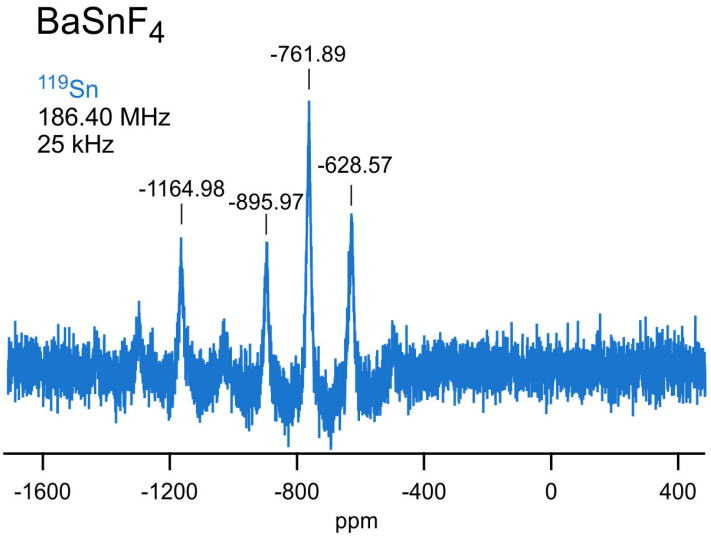

Fig. 3.26: ^{119}Sn-MAS NMR spectrum of $BaSnF_4$
(with 100 ppm = 18.6 kHz)

In this spectrum it is hard to distinguish between signal and associated satellites, as all lines offer a distance of 25 kHz from each other, which equals the rotation frequency. Most likely the lines at −1164.98 ppm and −761.89 ppm are actual signals, the remaining being side bands, as these are distributed very symmetrical around the two mentioned lines. This contradicts the fact that only one Sn position in $BaSnF_4$ should be present according to XRD data. In literature[9] only the line at −890 ppm is stated to be an actual signal, whereupon the measurement was carried out at a spinning speed at 17 kHz resulting in many additional spinning sidebands compared to this spectrum, making the interpretation even more difficult.

3.4 Fluorine Ion Battery

In the course of this work the synthesised F^--ion conductors were tested as solid state electrolyte with Li as anode and BiF_3 as cathode in the charged state, as well as in the discharged state with LiF as anode and Bi as cathode. As the use of $BaSnF_4$ did not result in any successful measurement, only the outcome of measurements with $La_{0.9}Ba_{0.1}F_{2.9}$ and $RbSn_2F_5$ are presented in this section.

3.4.1 Set-up Li - $La_{0.9}Ba_{0.1}F_{2.9}$ - BiF_3

In the following, the results of GCPL of the charged set-up with Li as anode, BiF_3 (milled with C65 and $La_{0.9}Ba_{0.1}F_{2.9}$) as cathode and $La_{0.9}Ba_{0.1}F_{2.9}$ as electrolyte are presented.

Three cells with identical weight of active materials and electrolyte, hence the same layer thicknesses, were build. Weight and thickness of all components are stated in Table 4.1 in the appendix. The diagrams which show the course of voltage versus time are illustrated in Fig. 3.27.

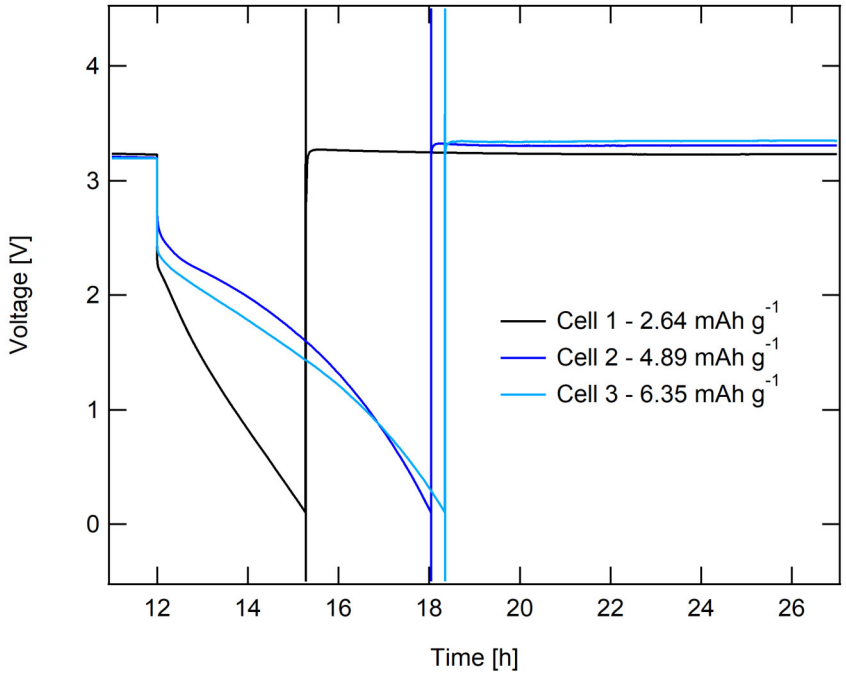

Fig. 3.27: Cell 1 to 3
FIB with $La_{0.9}Ba_{0.1}F_{2.9}$ as electrolyte, Li as anode and BiF_3 as cathode.
Voltage against time recorded at a temperature of 120 °C.

All cells could be discharged down to the set potential limit of 0.1 V. The specific discharge capacity in $mAh \cdot g^{-1}$ of the cells, stated in Fig. 3.27, is compared to a theoretical

value of $303\,\mathrm{mAh}\cdot\mathrm{g}^{-1}$ for BiF_3 extremely small (0.9 - 2.1 %). The low capacity might be explained by several factors, like a not completely depassivated Li-surface, various parameters of the conducting agent C65 or impurities in the cathode and electrolyte. Furthermore an insulating layer of LiF might form at the interface of electrolyte and Li-anode, inhibiting further charging of the cell.

In literature[35] a similar set-up with $Ba_{0.6}La_{0.4}F_{2.4}$ as electrolyte was reported to have a discharge capacity of $110\,\mathrm{mAh}\cdot\mathrm{g}^{-1}$. Even though this cell was operated at 150 °C with a different electrolyte, this does not explain the large discrepancy between the capacities of the cells.

There are some possibilities, which can be carried out to improve the performance of the cell, as another milling strategy to fabricate the cathode material, the usage of another conducting agent and a better depassivation of Li. To overcome the possible formation of LiF at the interface of electrolyte and anode, it was tried to fabricate a FIB in the discharged state with LiF as anode. To overcome conductivity issues in LiF, it was milled with electrolyte and C65.

3.4.2 Set-up LiF - $La_{0.9}Ba_{0.1}F_{2.9}$ - Bi

The reversed, discharged set-up with $La_{0.9}Ba_{0.1}F_{2.9}$ as electrolyte, LiF (milled with $La_{0.9}Ba_{0.1}F_{2.9}$ and C65) as anode and Bi (milled with $La_{0.9}Ba_{0.1}F_{2.9}$ and C65) as cathode was subjected to GCPL. At first it has to be noted that the pellet, completely composed out of compacted powders, was quite unstable and difficult to transfer into the Swagelok cell in one piece. If this step was successful, the cells often had a short circuit nonetheless. Finally three cells were subjected to GCPL. Out of these three cells, two only cycled extremely fast, in spite of the low currents applied, indicating a very low capacity. Their voltage vs. time plots are shown in the appendix (Fig. 4.5). The voltage vs. time plot of the relatively successful cell 1 is illustrated in Fig. 3.28.

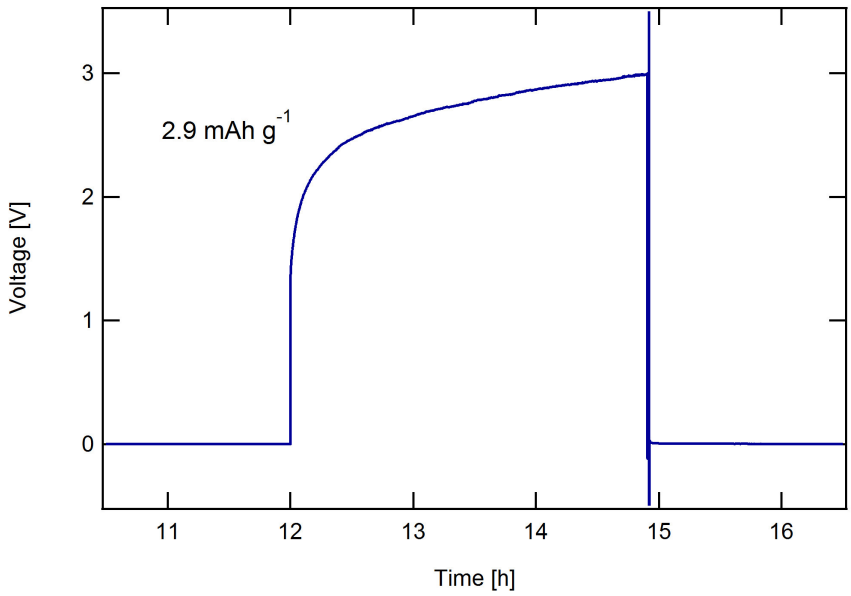

Fig. 3.28: Cell 1
FIB with $La_{0.9}Ba_{0.1}F_{2.9}$ as electrolyte, LiF as anode and Bi as cathode.
Voltage against time plot recorded at a temperature of 120 °C.

The plot shows one charging cycle, followed by very fast dis-/charging with capacities close to zero. The first charging offered a capacity of 2.9 mAh g^{-1}, which was far below the theoretical value (303 mAh g^{-1}). Apparently the strategy to reverse the set-up and hence inhibit the formation of LiF at the interface was not successful.

3.4.3 Set-up Li - $RbSn_2F_5$ - BiF_3

In this section the results of the GCPL of the FIB with Li as anode, BiF_3 (milled with C65 and $RbSn_2F_5$) as cathode and $RbSn_2F_5$ as electrolyte are presented.

Three cells with the same weight of active materials and electrolyte, hence the same layer thickness, were build. Weight and thickness of all components are enlisted in Table 4.1 in the appendix. As all three cells were showing similar cycling behaviour and capacities, only the voltage vs. time and capacity vs. cycle number plot of cell 3 is shown in Fig. 3.29 and Fig. 3.30. The corresponding plots of cell 1 and 2 are illustrated in the appendix (Fig. 4.6, 4.7, 4.8 and 4.9).

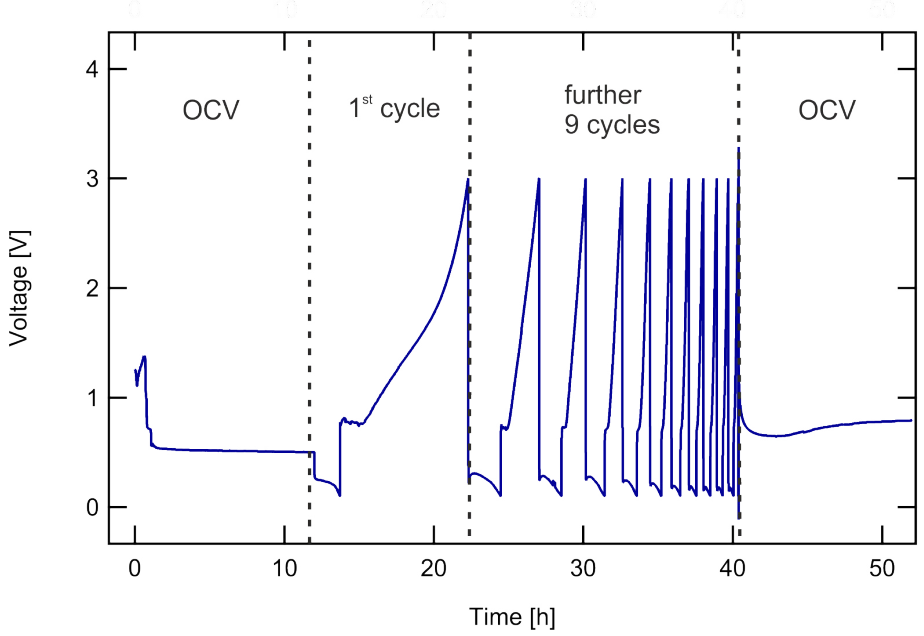

Fig. 3.29: Cell 3
FIB with $RbSn_2F_5$ as electrolyte, Li as anode and BiF_3 as cathode.
Voltage against time recorded at a temperature of 120 °C.

Before a current was applied, the OCV of the cell was measured for 12 hours. The OCV shows at first a voltage increase to 1.4 V followed by an abrupt decrease to 0.5 V. All three cells showed a similar behaviour in this section, which might be due to a reaction of the electrolyte at elevated temperatures with the active materials, at which Li is most probable the reaction partner due to its high reactivity. A redox reaction of the electrolyte is indicated by CV too.

After the OCV the cell was discharged down to a potential of 0.1 V. Beginning with cycle two, the potential dropped abruptly from 3 V down to approximately 0.2 V, before rising slightly and dropping finally while being discharged. The slight rising of the curve indicates that it took a certain time and current to reduce Bi^{+III} to Bi^0, which is a much better electrical conductor. While charging again a steep increase of potential to 0.7 V occurs, whereby kind of a potential plateau occurs. A reaction of the active material might be the reason for that too. Already by looking at the lapse of time for every cycle, it becomes apparent that the capacity decreases with every cycle.

The discharge as well as the charge capacity was calculated for every cycle and is illustrated in Fig. 3.30.

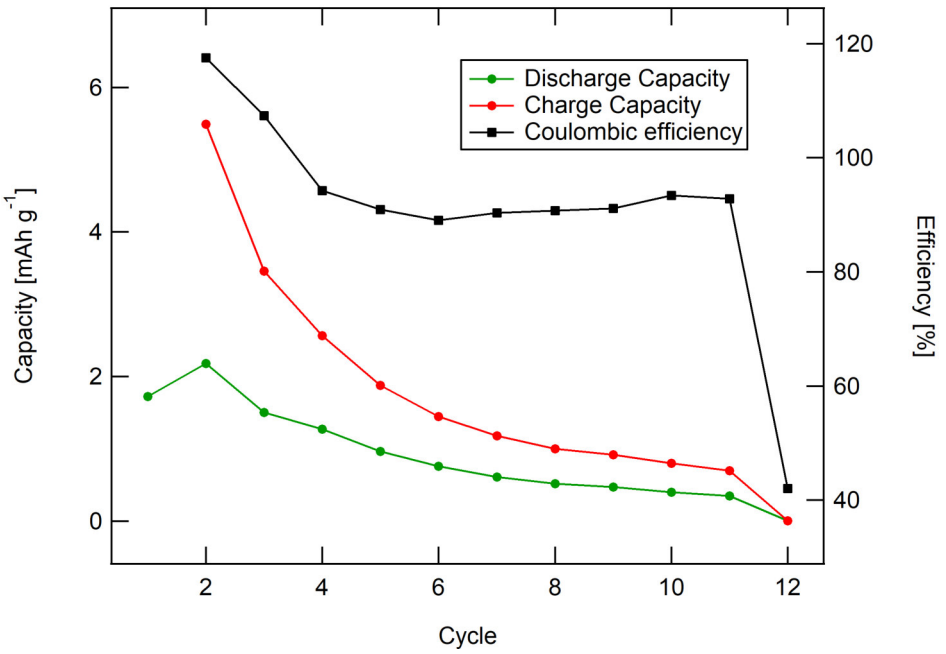

Fig. 3.30: Cell 3
FIB with $RbSn_2F_5$ as electrolyte, Li as anode and BiF_3 as cathode.
Capacity against cycle number recorded at a temperature of 120 °C.

Again the specific capacity is far below the theoretical value (303 mAh g^{-1}) and fades quickly, becoming zero when the current is increased from $\pm 12\,\mu$A to $\pm 24\,\mu$A. As the electrolyte is assumed to react before the GCPL is started, it is difficult to assume which reactions occur while cycling.

The coulombic efficiency η in %, presented in Fig. 3.30 too, was calculated with Eq. 3.3.

$$\eta = \frac{Q_{discharge}}{Q_{charge}} \cdot 100 \tag{3.3}$$

The efficiency lies above 100 % for the first two complete dis-/charging cycles, before dropping down to a constant value of 90 % for the next 8 cycles. The efficiency above 100 % might be explained by a self-discharge of the cell.

3.4.4 Set-up LiF - $RbSn_2F_5$ - Bi

The reversed, discharged set-up with $RbSn_2F_5$ as electrolyte, LiF as anode and Bi as cathode was build. Unfortunately the pressed pellets were unstable in all cases, resulting in short circuits.

4 Conclusion and Outlook

In the course of this work three F^--ion conductors, namely $BaSnF_4$, $RbSn_2F_5$ and $La_{0.9}Ba_{0.1}F_{2.9}$ were successfully synthesised. The gained structures were determined via XRD and furthermore impedance spectroscopy was carried out to quantify the conductivity. As the electric conductivity is of particular importance if the F^--ion conductors are used as solid state electrolytes in FIBs, it was measured via DC polarisation, with the outcome that the electrical conductivity is in all conductors orders of magnitude lower than the ionic conductivity. The electrochemical stability was further tested via CV, outlining that only $La_{0.9}Ba_{0.1}F_{2.9}$ is stable between -3 and $2\,V$.

To further investigate the ionic mobility in the samples, ^{19}F-MAS NMR was carried out and if possible, additionally ^{119}Sn- and ^{87}Rb-MAS NMR. T_1 and $T_{1\rho}$ of $RbSn_2F_5$ was measured and the jump rate was calculated.

The synthesised F^--ion conductors were used as solid state electrolytes in different active material combinations, with quite diverse performances. $BaSnF_4$ was not suited as electrolyte, as no dis-/charging was achieved. In all combinations it was possible to discharge or charge the FIBs with $La_{0.9}Ba_{0.1}F_{2.9}$ as electrolyte once. Irreversible reactions inhibited a reversible dis-/charging. Surprisingly $RbSn_2F_5$ was found to allow reversible dis-/charging with Li as anode and BiF_3 as cathode, in spite of or, just because the electrolyte reacted with the active materials before a current was applied. Even if the capacities did not reached theoretical values, it was able to demonstrate the function of a reversible working FIB, which was prior to that only published three times in literature.

The F^--ion conductors were tested with respect to structure, conductivity and stability already to a quite large extent. T_1 and $T_{1\rho}$ of $BaSnF_4$ could be measured in future, making a calculation of the jump rate in this compound possible. Furthermore a cell could be developed, allowing three-electrode solid state CV. Here it would be also interesting to subject $RbSn_2F_5$ to CV in a larger potential range, in order to investigate if Sn^0 forms then. Concerning FIBs a possibility to improve the reversibility and capacity could be the synthesis of a Li-Sn-alloy, which might develop at the interface of Li and $RbSn_2F_5$, making reversible cycling possible in the tested FIBs.

Bibliography

[1] M.M. Ahmad, K. Yamada, and T. Okuda. "Frequency dependent conductivity and dielectric studies on RbSn2F5". In: *Solid State Communications* 123 (2002), pp. 185–189.

[2] Mohamad M. Ahmad, Koji Yamada, and Tsutomu Okuda. "Conductivity spectra and comparative scaling studies of polycrystalline PbSnF4". In: *Solid State Ionics* 167 (2004), pp. 285–292.

[3] Mohamad M. Ahmad, Koji Yamada, and Tsutomu Okuda. "Ionic conduction and relaxation in KSn2F5 fluoride ion conductor". In: *Physica B: Condensed Matter* 339 (2003), pp. 94–100.

[4] Mohamad M. Ahmad, Yohei Yamane, and Koji Yamada. "Structure, ionic conduction, and giant dielectric properties of mechanochemically synthesized BaSnF4". In: *Journal of Applied Physics* 106 (2009), p. 074106.

[5] V. S. Bagotsky. *Fundamentals of Electrochemistry*. 2nd editio. New Jersey: John Wiley & Sons, Inc., 2006.

[6] Evgenij Barsoukov and J.Ross Macdonald. *Impedance Spectroscopy - Theory, Experiment, and Applications*. 2nd editio. Hoboken, New Jersey: John Wiley & Sons, Inc., 2005.

[7] J. P. Battut et al. "NMR and electrical conduction study of fluorine motion in MSn2F5 compounds with M=Na, K, Rb, Cs, Tl, NH4". In: *Solid State Ionics* 22 (1987), pp. 247–252.

[8] A.V. Chadwick et al. "Studies of Ionic Transport in MF2-SnF2 Systems". In: *Cryst. Latt. Def. and Amorph. Mat.* 15 (1987), pp. 303–308.

[9] Santanu Chaudhuri, Francis Wang, and Clare P. Grey. "Resolving the different dynamics of the fluorine sublattices in the anionic conductor BaSnF4 by using high-resolution MAS NMR techniques". In: *Journal of the American Chemical Society* 39 (2002), pp. 11746–11757.

[10] R. M. Dell. "Batteries - fifty years of materials development". In: *Solid State Ionics* 134 (2000), pp. 139–158.

[11] J.D. Donaldson and J.D. O'Donoghue. "Complex Tin(II) Fluorides". In: *Journal of Chemical Society* (1962), pp. 271–275.

[12] Melinda Duer. *Solid-state NMR spectroscopy - Principles and Applications*. Oxford: Blackwell Science, 2002, p. 567.

[13] Jeppe C. Dyre et al. "Fundamental questions relating to ion conduction in disordered solids". In: *Reports on Progress in Physics* 72 (2009), p. 046501. arXiv: 0803.2107.

[14] Martin Ermrich and Detlef Opper. *XRD for the analyst - Getting acquainted with the principles*. PANalytical GmbH, Kassel, 2011.

[15] Horst Friebolin. *Basic One- and Two-Dimensional NMR Spectroscopy*. 5th editio. Wiley-VCH Verlag GmbH&Co. KGaA, Weinheim, 2011.

[16] P.J. Gellings and H.J.M. Bouwmeester, eds. *The CRC Handbook of Solid State Electrochemistry*. CRC Press, Inc., 1997.

[17] Rudolf Gross and Achim Marx. *Festkörperphysik*. 2nd editio. Walter de Gruyter GmbH, Berlin/Boston, 2014.

[18] Udo Groß et al. "19F-NMR solid state investigations of monovalent alkali metal fluorides and tetra-alkylammonium fluorides". In: *Journal of Fluorine Chemistry* 115.2 (2002), pp. 193–199.

[19] F. Gschwind, Z. Zhao-Karger, and M. Fichtner. "Fluoride-doped PEG matrix as an electrolyte for anion transportation in a room-temperature fluoride ion battery". In: *Journal of Materials Chemistry A* 2.5 (2014), pp. 1214–1218.

[20] F. Gschwind et al. "Fluoride ion batteries: Theoretical performance, safety, toxicity, and a combinatorial screening of new electrodes". In: *Journal of Fluorine Chemistry* 182 (2016), pp. 76–90.

[21] Carl H. Hamann and Wolf Vielstich. *Elektrochemie*. 4th editio. Weinheim: Wiley-VCH Verlag GmbH&Co. KGaA, 2005, p. 662.

[22] Malcolm H Hebb. "Electrical Conductivity of Silver Sulfide". In: *J. Chem. Phys.* 20.1 (1952), pp. 185–190.

[23] John H Kennedy and James C Hunter. "Thin-Film Galvanic Cell Pb/PbF2/PbF2,CuF2/Cu". In: *J. Electrochem. Soc.* 123.1 (1976), pp. 10–14.

[24] Harald Krischner and Brigitte Koppelhuber-Bitschnau. *Röntgenstrukturanalyse und Rietveldmethode*. 5th editio. Friedr. Vieweg & Sohn Verlagsgesellschaft mbH, Braunschweig/Wiesbaden, 1994.

[25] P. Padma Kumar and S. Yashonath. “Ionic Conduction in the Solid State”. In: *Journal of Chemical Science* 118.1 (2006), pp. 135–154.

[26] Vadim F. Lvovich. *Impedance Spectroscopy - Applications to Electrochemical and Dielectric Phenomena*. Hoboken, New Jersey: John Wiley & Sons, Inc., 2012.

[27] Jung-Ki Park. *Principles and Applications of Lithium Secondary Batteries*. Weinheim: Wiley-VCH Verlag GmbH&Co. KGaA, Weinheim, 2012.

[28] L. N. Patro and K. Hariharan. “Influence of synthesis methodology on the ionic transport properties of BaSnF4”. In: *Materials Research Bulletin* 46 (2011), pp. 732–737.

[29] Laxmi Narayana Patro and K. Hariharan. “Frequency dependent conduction characteristics of mechanochemically synthesized NaSn2F5”. In: *Materials Science and Engineering B: Solid-State Materials for Advanced Technology* 162 (2009), pp. 173–178.

[30] Tatyana Polenova, Rupal Gupta, and Amir Goldbourt. “Magic angle spinning NMR spectroscopy: A versatile technique for structural and dynamic analysis of solid-phase systems”. In: *Analytical Chemistry* 87.11 (2015), pp. 5458–5469.

[31] Florian Preishuber-Pflügl. “Access to Nanocrystalline F-Ion Conductors by Mechanochemistry: Insights into Synthesis Conditions and Diffusion Parameters”. Dissertation. Technical University Graz, 2016, p. 125.

[32] Florian Preishuber-Pflügl and Martin Wilkening. “Mechanochemically synthesized fluorides: local structures and ion transport”. In: *Dalton Trans.* 45 (2016), pp. 8675–8687.

[33] M. Anji Reddy and M. Fichtner. “Batteries based on fluoride shuttle”. In: *Journal of Materials Chemistry* 21 (2011), pp. 17059–17062.

[34] C. Rongeat et al. “Development of new anode composite materials for fluoride ion batteries”. In: *Journal of Materials Chemistry A* 2.48 (2014), pp. 20861–20872.

[35] Carine Rongeat et al. “Nanostructured Fluorite-type Fluorides as Electrolyte for Fluoride Ion Batteries”. In: *The Journal of Physical Chemistry C* 117 (2013), pp. 4943–4950.

[36] Carine Rongeat et al. “Solid Electrolytes for Fluoride Ion Batteries : Ionic Conductivity in Polycrystalline Tysonite-Type Fluorides”. In: *ACS Appl. Mater. Interfaces* 6 (2014), pp. 2103–2110.

[37] J. Schoonman. “A Solid-State Galvanic Cell with Fluoride-Conducting Electrolytes”. In: *Journal of The Electrochemical Society* 123.12 (1976), pp. 1772–1775.

[38] S. Vilminot, R. Bachmann, and H. Schulz. “Structure and conductivity in KSn2F5”. In: *Solid State Ionics* 9-10 (1983), pp. 559–562.

[39] K. Yamada et al. “Two dimensional fluoride ion conductor RbSn2F5 studied by impedance spectroscopy and 19F, 119Sn, and 87Rb NMR”. In: *European Physical Journal B* 40.2 (2004), pp. 167–176.

[40] Le Zhang, Munnangi Anji Reddy, and Maximilian Fichtner. “Development of tysonite-type fluoride conducting thin film electrolytes for fluoride ion batteries”. In: *Solid State Ionics* 272 (2015), pp. 39–44.

[41] Le Zhang et al. “Development of dense solid state thin-film electrolyte for fluoride ion batteries”. In: *Journal of Alloys and Compounds* 684 (2016), pp. 733–738.

Figures

Tables

Additional Information

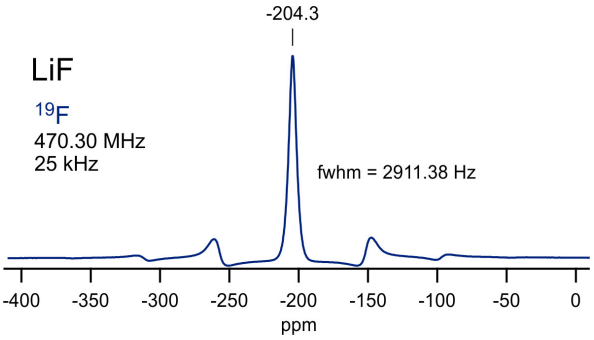

Fig. 4.1: ^{19}F-MAS NMR spectra of LiF used as reference for all ^{19}F-MAS NMR spectra

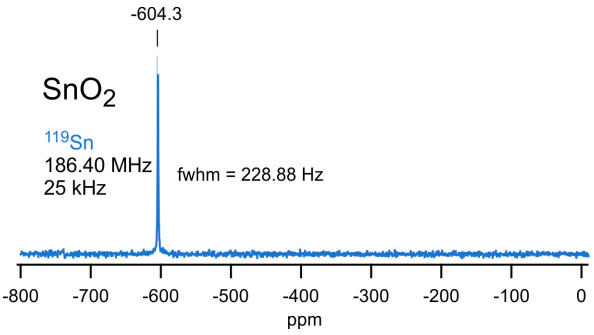

Fig. 4.2: ^{119}Sn-MAS NMR spectra of SnO_2 used as reference for all ^{119}Sn-MAS NMR spectra

Table 4.1: Overview of all assembled cells.

Cell	**Weight / Thickness Electrolyte**	**Weight Cathode**	**Weight Anode**	**Comment**
BiF_3 - $BaSnF_4$ - Li-1	70.49 mg ~420 μm	70.44 mg (21.13 mg BiF_3)	~5.5 mg	difficulties within the first dicharge
BiF_3 - $BaSnF_4$ - Li-2	70.20 mg ~420 μm	70.70 mg (21.21 mg BiF_3)	~5.5 mg	no discharge
BiF_3 - $BaSnF_4$ - Li-3	70.00 mg ~420 μm	62.8 mg (18.84 mg BiF_3)	~5.5 mg	no discharge

BiF_3 - $La_{0.9}Ba_{0.1}F_{2.9}$ - Li-1	99.40 mg ~600 μm	40.5 mg (12.15 mg BiF_3)	~5.5 mg	one discharge
BiF_3 - $La_{0.9}Ba_{0.1}F_{2.9}$ - Li-2	99.30 mg ~600 μm	40.2 mg (12.06 mg BiF_3)	~5.5 mg	one discharge
BiF_3 - $La_{0.9}Ba_{0.1}F_{2.9}$ - Li-3	100.40 mg ~600 μm	39.98 mg (11.99 mg BiF_3)	~5.5 mg	one discharge
BiF_3 - $RbSn_2F_5$ - Li-1	99.71 mg ~670 μm	40.2 mg (12.06 mg BiF_3)	~5.5 mg	10 cycles
BiF_3 - $RbSn_2F_5$ - Li-2	80.45 mg ~540 μm	41.22 mg (12.36 mg BiF_3)	~5.5 mg	7 cycles
BiF_3 - $RbSn_2F_5$ - Li-3	81.02 mg ~540 μm	40.05 mg (12.02 mg BiF_3)	~5.5 mg	10 cycles
Bi - $La_{0.9}Ba_{0.1}F_{2.9}$ - LiF-1	50.02 mg ~260 μm	41.05 mg (12.32 mg BiF_3)	39.60 mg (11.88 mg LiF)	one charge
Bi - $La_{0.9}Ba_{0.1}F_{2.9}$ - LiF-2	59.95 mg ~300 μm	40.17 mg (12.05 mg BiF_3)	40.95 mg (12.28 mg LiF)	one charge (very fast)
Bi - $La_{0.9}Ba_{0.1}F_{2.9}$ - LiF-2	60.03 mg ~300 μm	41.20 mg (12.36 mg BiF_3)	40.02 mg (12.01 mg LiF)	one charge (very fast)

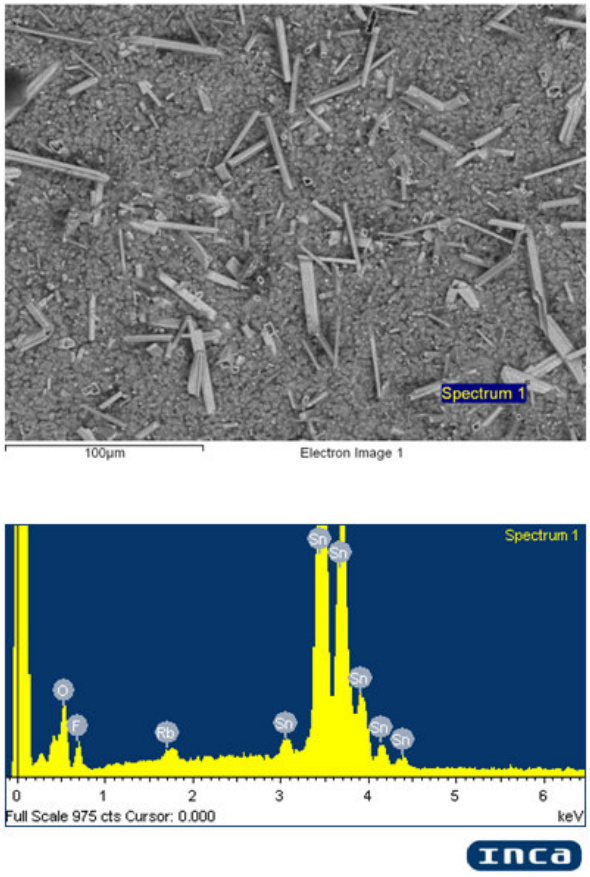

Fig. 4.3: EDX Spectrum of $RbSn_2F_5$ annealed at 538 K

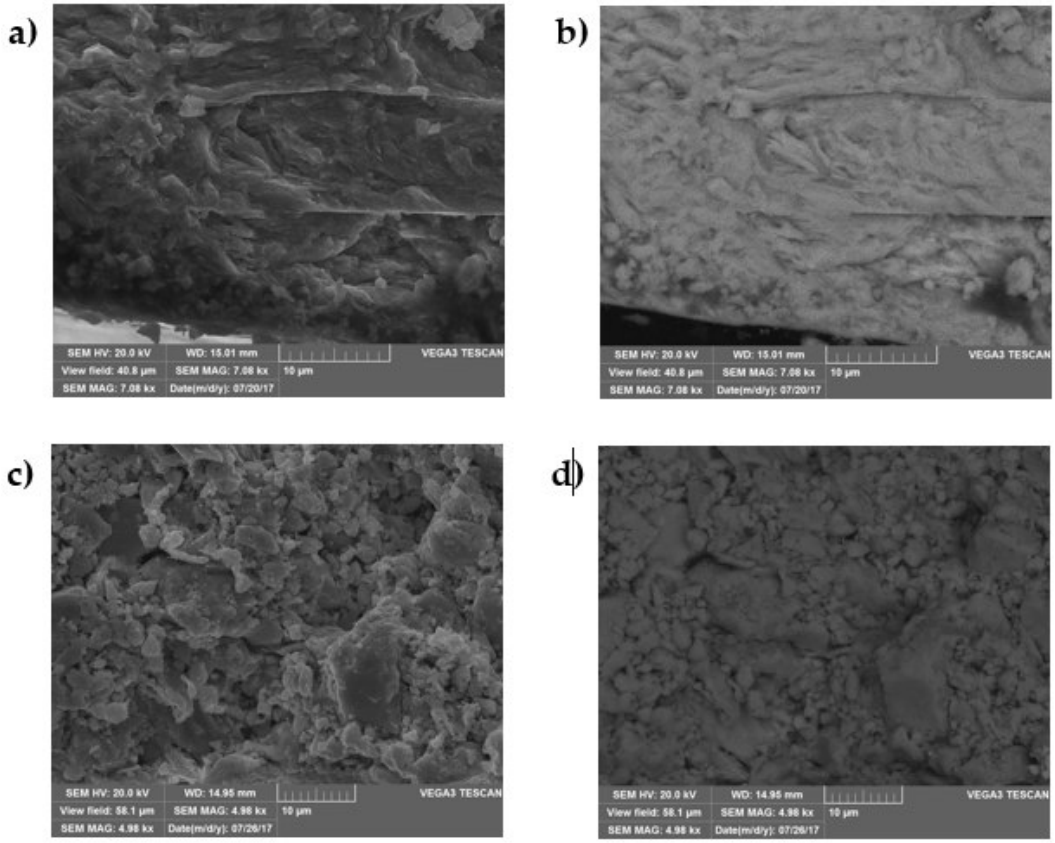

Fig. 4.4: SEM pictures of $RbSn_2F_5$
a) Before CV under 7.000 - fold magnification acquired with SE detector.
b) Before CV under 7.000 - fold magnification acquired with BSE detector.
c) After CV under 5.000 - fold magnification acquired with SE detector.
d) After CV under 5.000 - fold magnification acquired with BSE detector.

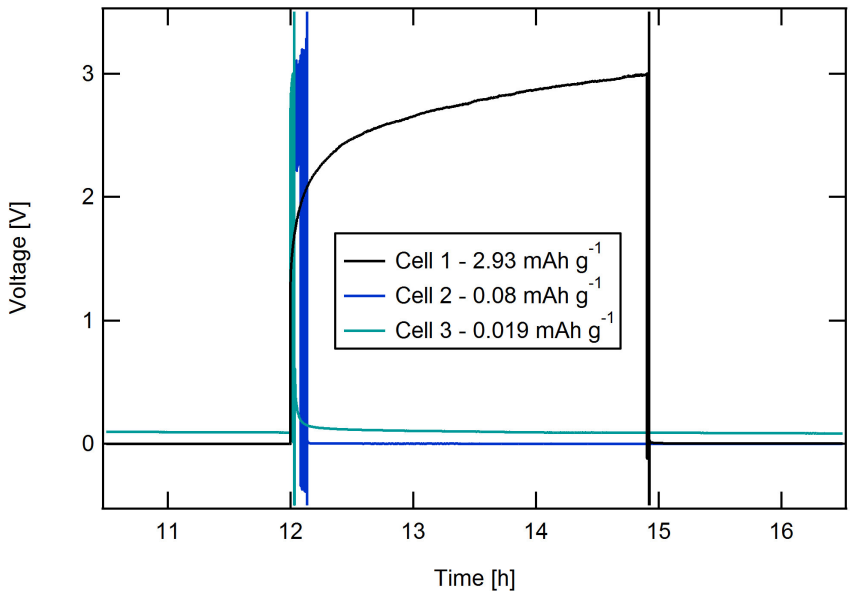

Fig. 4.5: Cell 1 - 3
FIB with $La_{0.9}Ba_{0.1}F_{2.9}$ as electrolyte in the charged set-up (LiF as anode, Bi as cathode).
Time against voltage plot recorded at a temperature of 120 °C.

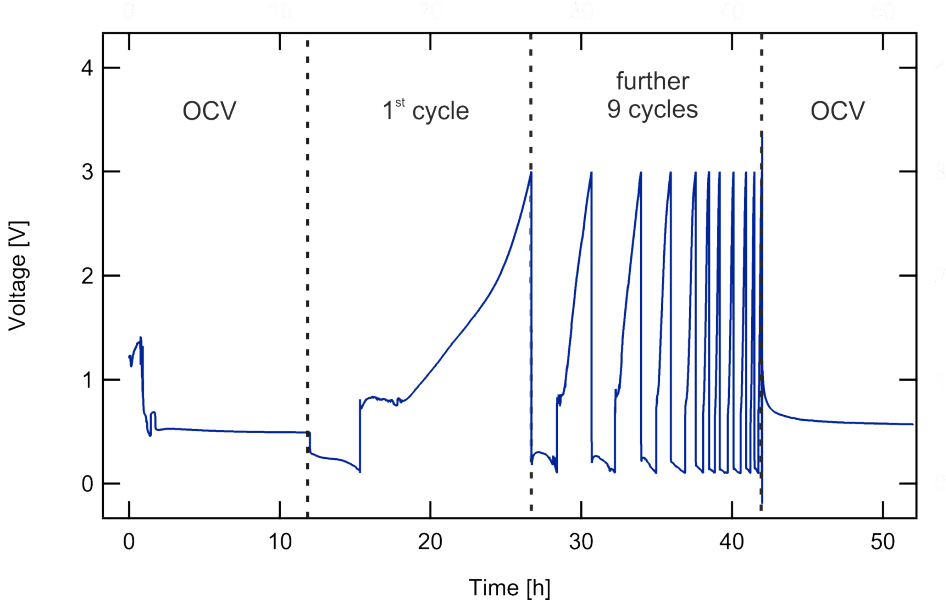

Fig. 4.6: Cell 1
FIB with $RbSn_2F_5$ as electrolyte, Li as anode and BiF_3 as cathode.
Time against voltage plot recorded at a temperature of 120 °C.

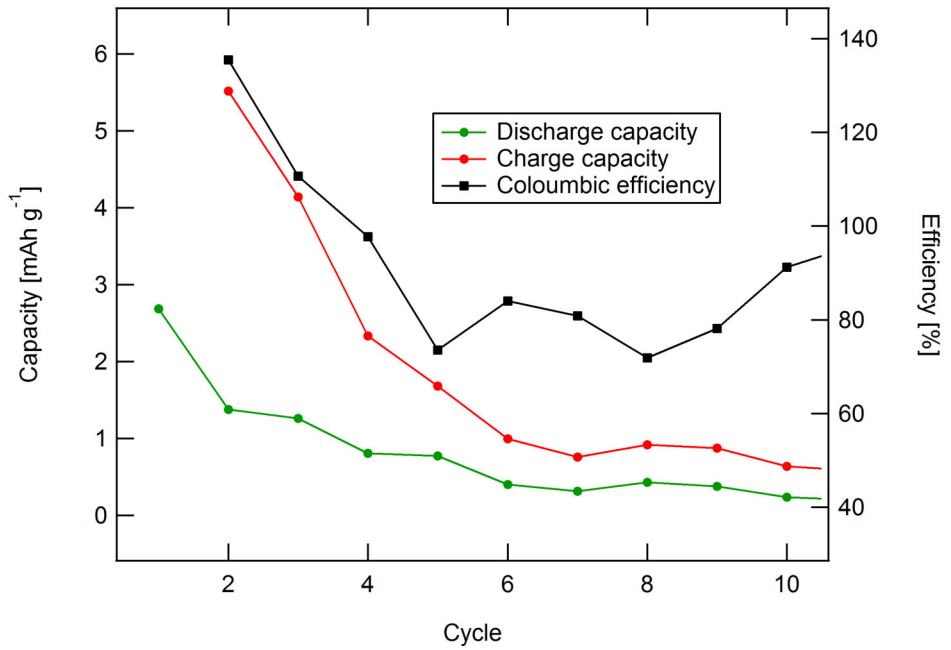

Fig. 4.7: Cell 1
FIB with $RbSn_2F_5$ as electrolyte, Li as anode and BiF_3 as cathode.
Capacity against cycle number recorded at a temperature of 120 °C.

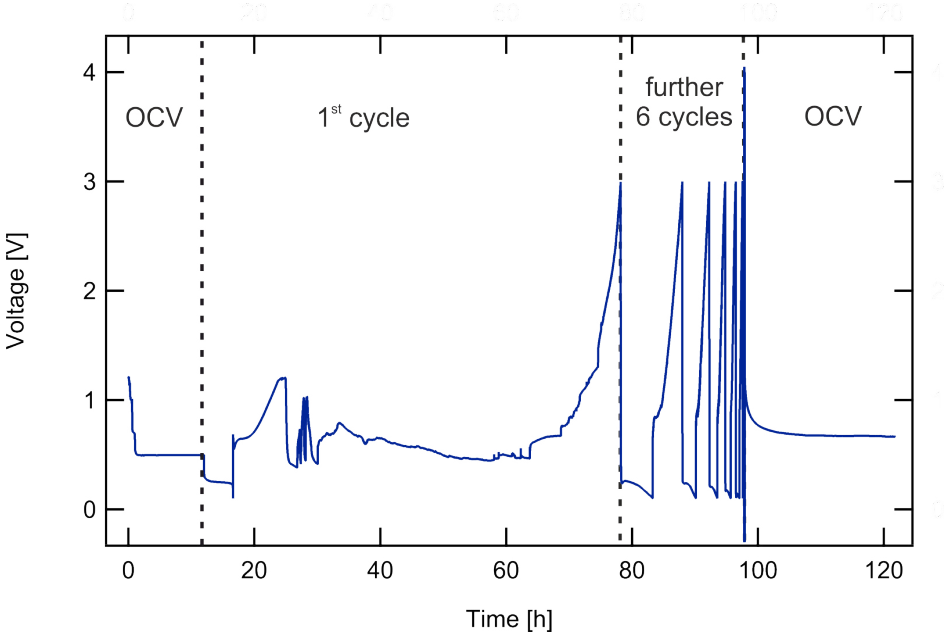

Fig. 4.8: Cell 2
FIB with $RbSn_2F_5$ as electrolyte, Li as anode and BiF_3 as cathode.
Time against voltage plot recorded at a temperature of 120 °C.

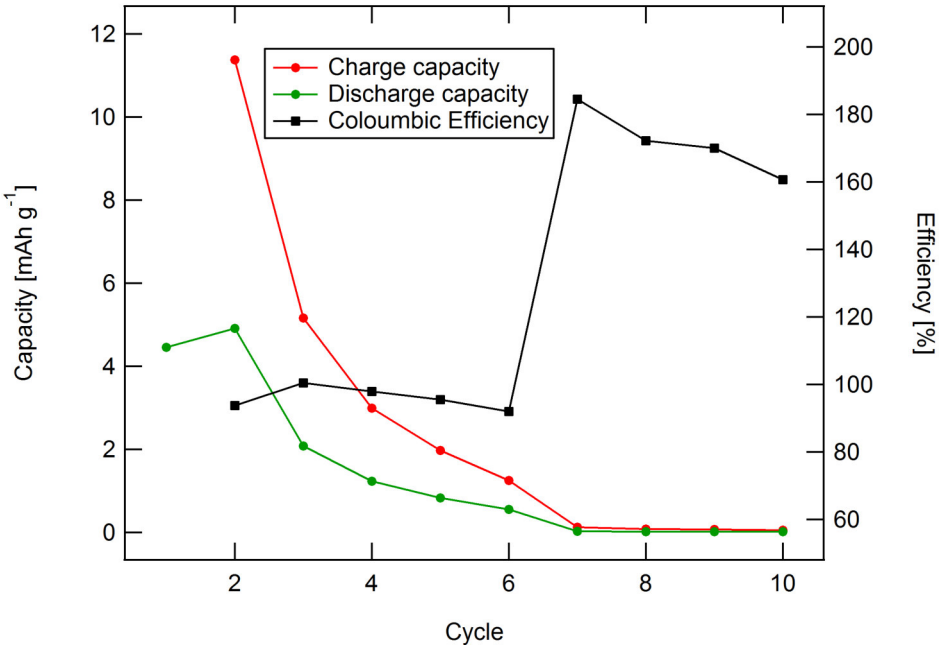

Fig. 4.9: Cell 2
FIB with $RbSn_2F_5$ as electrolyte, Li as anode and BiF_3 as cathode. Capacity against cycle number recorded at a temperature of 120 °C.